

Dual modulation of cytotoxic and checkpoint receptors tunes the efficacy of adoptive Delta One T cell therapy against colorectal cancer

Received: 16 May 2024

Accepted: 13 March 2025

Published online: 16 April 2025

 Check for updates

Rafael Blanco-Domínguez¹✉, Leandro Barros¹, Mariana Carreira¹, Manon van der Ploeg², Carolina Condeço¹, Gabriel Marsères³, Cristina Ferreira⁴, Carla Costa⁴, Carlos M. Ferreira⁴, Julie Déchanet-Merville^{5,6}, Noel F. C. C. de Miranda², Sofia Mensurado^{1,7} & Bruno Silva-Santos^{1,6,7}✉

Colorectal cancer (CRC) remains a challenge for current immunotherapies. $V\delta 1^+$ $\gamma\delta$ T cells offer a promising alternative because of their HLA-I-independent cytotoxicity and natural tissue tropism. We developed Delta One T (DOT) cells, a $V\delta 1^+$ $\gamma\delta$ T cell-based adoptive cell therapy clinically explored for hematological malignancies but not yet for solid tumors. Here we demonstrate the capacity of DOT cells to target CRC cell lines and patient-derived specimens and organoids in vitro and to control tumor growth in an orthotopic xenograft model of CRC. Notwithstanding, we found tumor-infiltrating DOT cells to exhibit a dysregulated balance of cytotoxic and inhibitory receptors that paralleled that of endogenous $V\delta 1^+$ tumor-infiltrating lymphocytes and limited their cytotoxicity. To maximize efficacy, we unveil two strategies, increasing targeting through upregulation of NKG2D ligands upon butyrate administration and blocking the checkpoints TIGIT and PD1, which synergistically unleashed DOT cell cytotoxicity. These findings support DOT cell-based combinatorial approaches for CRC treatment.

Colorectal cancer (CRC) is the second leading cause of cancer deaths worldwide (World Health Organization, 1 Feb 2024). Attempting to address the limitations of conventional treatments, immunotherapy has recently been applied to CRC but with very limited success. In fact, only around 10–15% of CRC cases, characterized by mismatch repair deficiency (MMR-d), microsatellite instability (MSI) and very high mutational burdens, encompass clinical responses to checkpoint inhibition¹, which underscores the need for novel immunotherapy approaches, particularly for MMR-proficient (MMR-p) and microsatellite-stable (MSS) CRC.

Immune checkpoint blockade (ICB) targeting the programmed death protein 1 (PD1)–PDL1 (PD1 ligand 1) axis is the best-established immunotherapy for solid cancers, having revolutionized the treatment of advanced melanoma and lung carcinoma². The mechanism of action of anti-PD1 ICB is presumably the functional release of tumor-specific $\alpha\beta$ T cell clones, especially cytotoxic CD8⁺ T cells capable of recognizing somatically mutated neoantigens presented on major histocompatibility class I (MHC-I) complexes. However, advanced tumors often escape CD8⁺ T cell surveillance by downregulating MHC-I presentation³.

¹Gulbenkian Institute for Molecular Medicine, Lisbon, Portugal. ²Department of Pathology, Leiden University Medical Center, Leiden, The Netherlands.

³University of Bordeaux, CNRS, ImmunoConcEpt, UMR 5164, Bordeaux, France. ⁴Hospital de Santa Maria, Centro Hospitalar Lisboa Norte, Lisbon, Portugal.

⁵Equipe labélisée LIGUE Contre le Cancer, Bordeaux, France. ⁶Faculdade de Medicina da Universidade de Lisboa, Lisbon, Portugal. ⁷These authors contributed equally: Sofia Mensurado, Bruno Silva-Santos.

✉ e-mail: rafael.blanco@gimm.pt; bssantos@medicina.ulisboa.pt

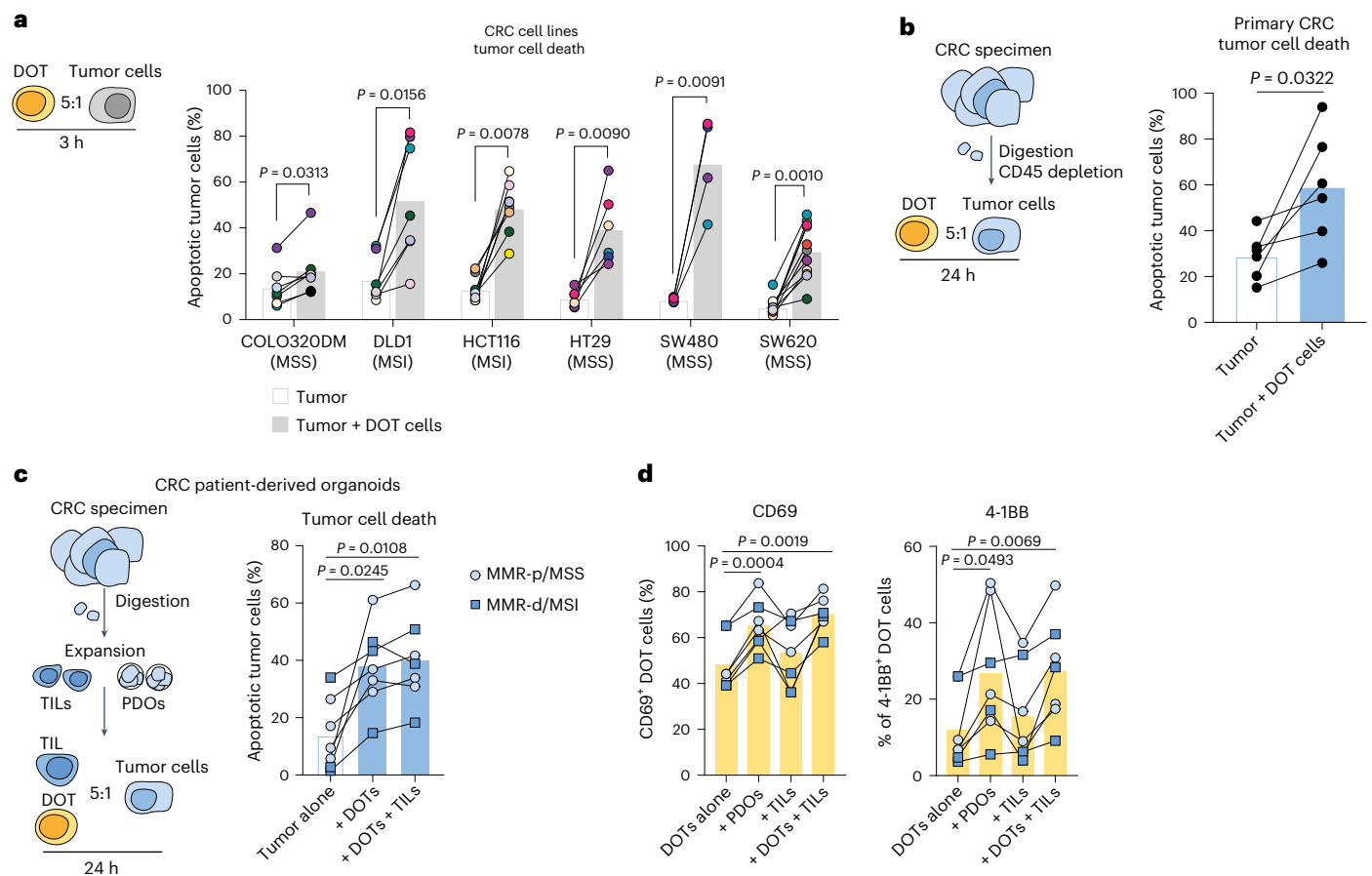


Fig. 1 | DOT cells target CRC in vitro. **a**, Schematic representation and tumor cell death quantification by annexin V in 3-h killing assays of DOT cells against different MSI and MSS CRC cell lines. Colors depict individual DOT donors (pool of 16 assays). Data were analyzed by a two-tailed paired *t*-test for normal distributions or Wilcoxon matched-pairs ranked test for nonnormal distributions. **b**, Schematic representation and DOT cell killing of CD45-depleted primary CRC tumor specimens, measured by caspase 3/7 staining. Lines connect specimens from the same participant ($n = 6$ participants, pool of five assays). Data were analyzed by a two-tailed paired *t*-test. **c**, Experimental layout and

percentage of apoptotic tumor cells (measured by caspase 3/7 green staining) in the presence or absence of allogeneic DOT cells and/or TILs from the same participants ($n = 7$ participants). Samples from participants with MMR-p/MSS and MMR-d/MSI CRC are represented as circles and squares, respectively. **d**, Expression of CD69 and 4-1BB by DOT cells in the presence or absence of PDOs and/or TILs. Lines connect data points from the same participants ($n = 7$ participants). In **c** and **d**, data are a pool of four different assays and were analyzed by a repeated-measures one-way ANOVA with Holm–Šidák’s multiple-comparisons test.

Specifically, mutational interference with the key MHC-I component, $\beta 2$ microglobulin (*B2M*), was observed in MMR-d CRC tumors, leading to a striking expansion of cytotoxic $\gamma\delta$ (instead of $\alpha\beta$) T cells⁴. In fact, imaging mass cytometry analysis of wild-type and mutant *B2M* CRC samples before and after PD1 blockade identified $\gamma\delta$ T cells to be the only immune subset significantly enriched in ICB-treated mutant *B2M* compared to wild-type *B2M* cancers. Interestingly, $V\delta 1^+$ T cells were the dominant tumor-infiltrating $\gamma\delta$ T cell population in CRC and a fraction of these expressed PD1 concomitantly with activating natural killer cell receptors (NKR) such as NKp46 and NKG2D, as well as cytotoxic (granzyme B and perforin) and proliferation markers⁴. This phenotype was reminiscent of a previous study identifying an NKp46⁺ $V\delta 1^+$ T cell subset in the intestinal epithelium with enhanced cytotoxicity against CRC⁵, thus pointing to NKR-expressing $V\delta 1^+$ $\gamma\delta$ T cells as important antitumor effectors in CRC.

$V\delta 1^+$ $\gamma\delta$ T cells have been recently associated with good prognosis in various cancer types, including lung⁶ and breast⁷ carcinomas and melanoma⁸. Furthermore, assessment of 557 persons with CRC showed that those with more abundant $\gamma\delta$ tumor-infiltrating lymphocytes (TILs) had better 5-year disease-free survival⁹. This was consolidated in a subsequent RNA-sequencing analysis of 620 CRC and 51 paraneoplastic samples, which indicated that the extent of $\gamma\delta$ T cell infiltration

but not that of CD8⁺ T cells or NK cells positively correlated with the overall survival of persons with the MSS subtype of CRC¹⁰. In all these studies^{4,5,9}, the majority of $\gamma\delta$ T cells infiltrating CRC lesions were clearly $V\delta 1^+$ T cells, which, together with their potent cytotoxic functions in vitro^{4,5} and in vivo¹¹ preclinical models of CRC, suggest great potential as effectors for next-generation immunotherapies^{12,13}. However, a selective $V\delta 1^+$ $\gamma\delta$ T cell-based strategy for CRC is still to be tested in the clinic.

We developed Delta One T (DOT) cells as a clinical-grade $V\delta 1^+$ $\gamma\delta$ T cell-based product for adoptive cell therapy^{12,14}. We coupled a pioneering $V\delta 1^+$ $\gamma\delta$ T cell-biased expansion protocol with the differentiation of cytotoxic effector cells expressing high levels of NKR^{14,15} and demonstrated the ability of the final cell product to efficiently target lymphoid^{14,15} and myeloid^{16,17} leukemias. This body of evidence on DOT cells enabled a clinical program in acute myeloid leukemia (AML; [NCT05886491](https://clinicaltrials.gov/ct2/show/study/NCT05886491)).

Here, we investigated the therapeutic potential of DOT cells against solid tumors, focusing on preclinical models of CRC. We show that DOT cells are broadly reactive to both MSI and MSS CRC cell lines, as well as to CRC tumor material and patient-derived organoids (PDOs) in vitro. Although the anti-CRC functions of DOT cells were also evident in an orthotopic xenograft model of human CRC, they were seemingly constrained by a dysregulated balance of cytotoxic and inhibitory

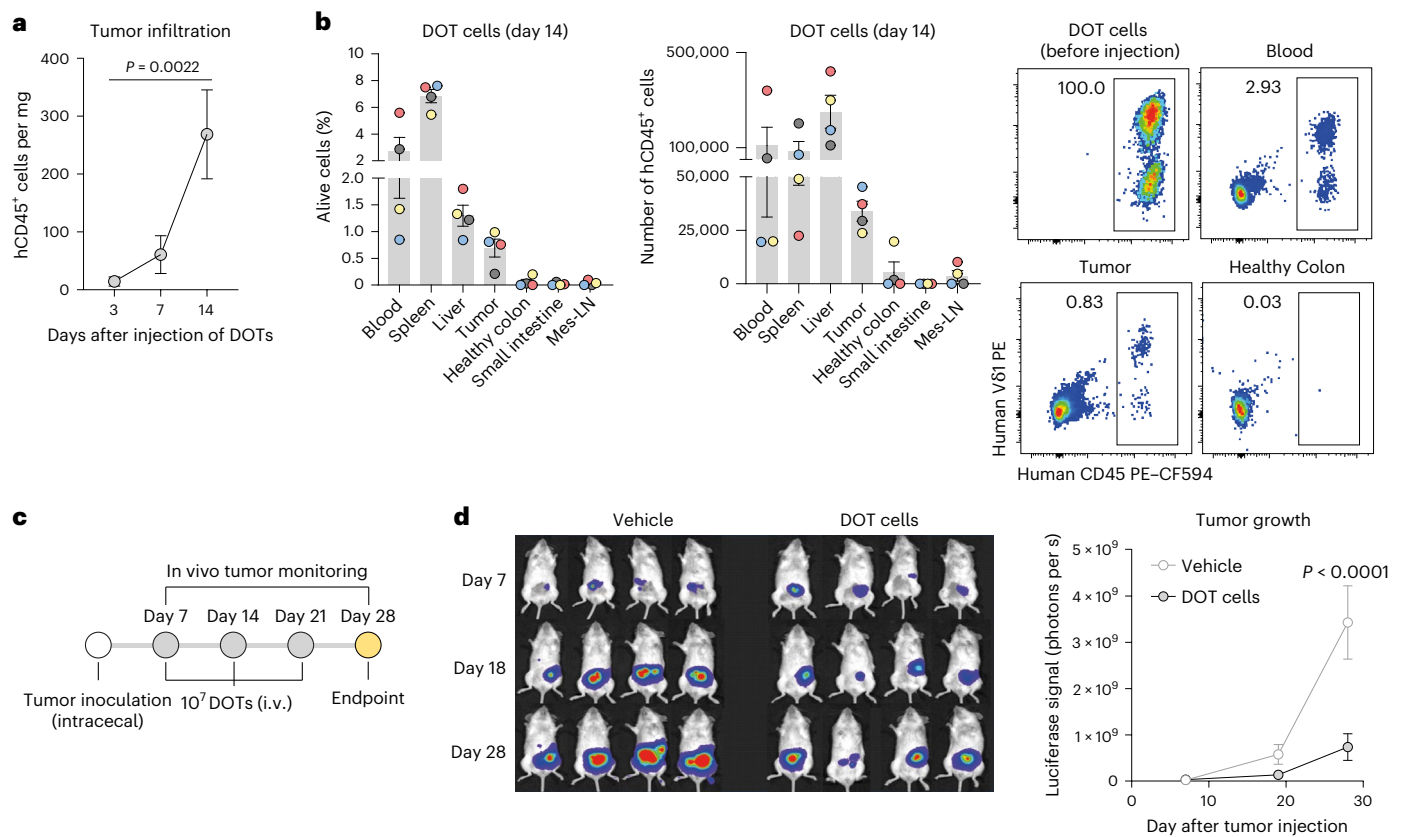


Fig. 2 | DOT cells control CRC growth in vivo. **a**, Kinetics of tumor-infiltrating DOT cell numbers, per milligram of SW620 tumor tissue, assessed by human CD45 expression by flow cytometry at day 3 ($n = 6$ mice), day 7 ($n = 7$ mice) and day 14 ($n = 11$ mice) after one infusion with 10 million cells. Data were analyzed by a one-way ANOVA with Tukey's post hoc test. **b**, Representative flow cytometry density plots with percentages after gating on alive cells and quantification of percentages (of human CD45⁺ within alive cells) and numbers of DOT cells in tumor and different organs. Colors represent individual mice ($n = 4$ mice).

c, Experimental layout of in vivo i.v. infused DOT cell treatment in an orthotopic (intracecal injection of SW620 cells) CRC model. **d**, Representative images and kinetics of in vivo tumor growth, quantified as luciferase signal by IVIS lumina ($n = 8$ mice per group). Data were analyzed by a repeated-measures two-way ANOVA with Šidák's multiple-comparisons test. In **a**, **b** and **d**, data are presented as the means \pm s.e.m. and correspond to one representative of three independent experiments with similar results.

receptors. Importantly, we devised two strategies to overcome this limitation, one based on the key stimulatory role of NKG2D and its ligands and the other based on the synergistic inhibitory function of T cell immunoreceptor with Ig and ITIM domain (TIGIT) and PD1, thereby paving the way for DOT cell-based combinatorial approaches for CRC treatment.

Results

DOT cells target CRC in vitro and in vivo

We started this study by assessing the anti-CRC cytotoxic activity of DOT cells, which were expanded and differentiated as previously reported^{14,16,18}. As expected, DOT products were composed of $\gamma\delta$ T cells with a major bias for V δ 1⁺ cells and minor fractions of V δ 2⁺ and V δ 1⁻V δ 2⁻ $\gamma\delta$ T cells (Extended Data Fig. 1a) and expressed multiple NKR (namely, NKG2D, DNAM1/CD226 and, to a lesser extent, NKp30) (Extended Data Fig. 1b). Importantly, DOT cells showed striking degranulation (CD107a/LAMP1) potential associated with high expression of cytolytic molecules (granzyme B and perforin) and displayed a type 1 (interferon- γ (IFN γ) and tumor necrosis factor (TNF)) cytokine profile upon activation (Extended Data Fig. 1c). During a 3-h coincubation with CRC targets, we found DOT cells to form immune synapses (Extended Data Fig. 2) and to kill (Fig. 1a) both MSI and MSS CRC cell lines, thus revealing broad reactivity against CRC independently of the microsatellite status. Furthermore, DOT cells showed strong cytotoxicity against primary CD45-depleted primary CRC biopsies (Fig. 1b) from a retrospective cohort of CRC in a 24-h killing assay. Because PDOs have emerged as

a more suitable in vitro model to replicate the influence of the tumor microenvironment (TME) and genetic landscape¹⁹, we conducted 24-h cytotoxicity assays using allogeneic DOT cells against PDOs derived from participants with both MMR-p/MSS and MMR-d/MSI CRC (Supplementary Table 1). Additionally, to assess the potential impact of endogenous immune cells, we performed these assays in the presence or absence of autologous expanded TILs from the same tumor samples. Notably, DOT cells induced potent killing of CRC PDOs irrespective of MMR status or presence of TILs (Fig. 1c). The broad reactivity of DOT cells against CRC was further indicated by the increased levels of the activation markers CD69 and 4-1BB on DOT cells upon coculture with both MMR-p/MSS and MMR-d/MSI CRC PDOs, independently of the presence of TILs (Fig. 1d).

An important challenge of current adoptive cell therapies is their limited capacity to infiltrate solid tumors²⁰. However, as V δ 1⁺ T cells have a natural tropism for the colon⁵ and have been found in CRC tumors⁹, we anticipated that intravenously (i.v.) infused DOT cells would have the capacity to infiltrate CRC tumors in vivo. To directly assess this, we established an orthotopic xenograft model of human CRC by implanting luciferase-positive SW620 cells in the cecum of immunocompromised NOG mice expressing human interleukin (IL)-15, which is necessary for DOT cell persistence in mice¹⁸. We let orthotopic CRC tumors grow and establish for 3 weeks in the cecum before injecting DOT cells i.v. We observed a clear infiltration and progressive accumulation of DOT cells within the tumors, thus demonstrating CRC homing in vivo (Fig. 2a). Importantly, biodistribution evaluation

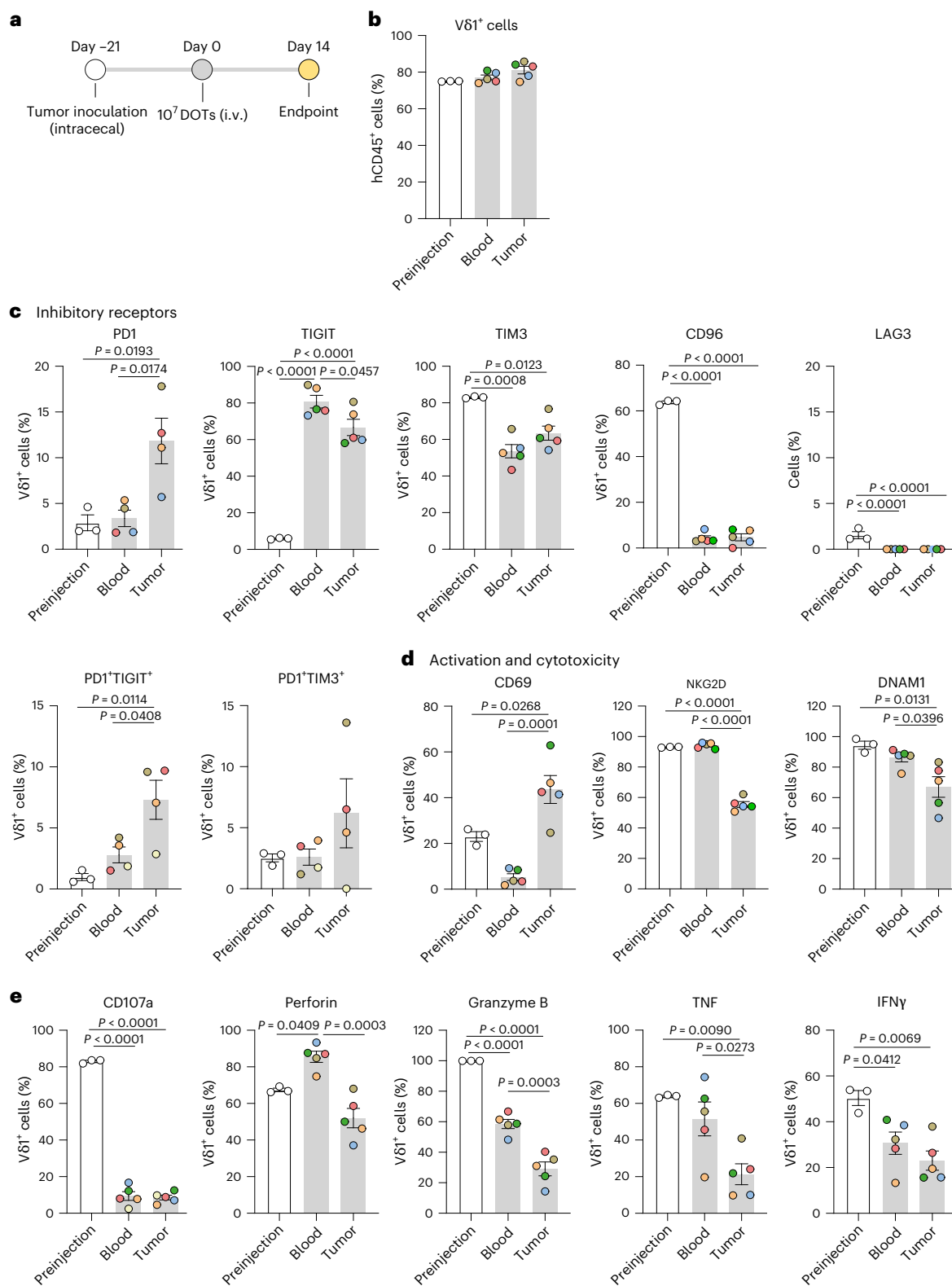
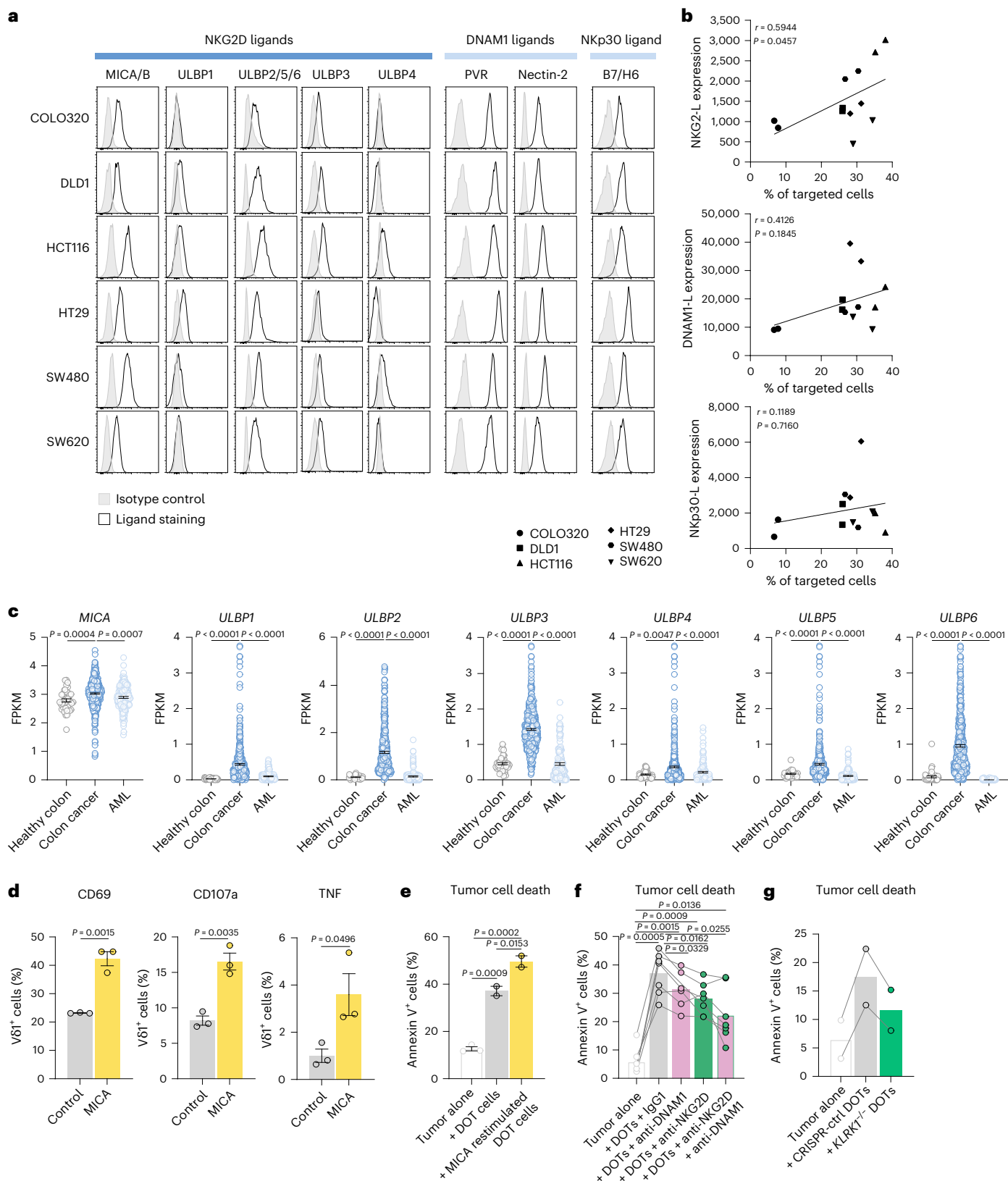


Fig. 3 | DOT cells exhibit compromised cytotoxicity within CRC tumors.
a, Schematic representation of the experimental approach to assess DOT cell phenotype upon their i.v. inoculation in intracecal SW620 tumor-bearing mice. **b–e**, Quantification of percentage of Vδ1 (**b**) and expression of immunomodulatory or checkpoint receptors (**c**), activation and cytotoxic receptors (**d**) and CD107a and intracellular markers (**e**) after 3 h of PMA and ionomycin stimulation (in the presence of protein translocation inhibitors) on

DOT cells before infusion ($n = 3$ technical replicates) to mice and in blood and tumor ($n = 4$ mice for PD1, PD1⁺TIGIT⁺ and PD1⁺TIM3⁺; $n = 5$ mice for the rest), represented as a percentage of alive human CD45⁺CD3⁺Vδ1⁺ cells and assessed by flow cytometry. In **b–e**, colors represent individual mice. Data are presented as the means \pm s.e.m. Data were analyzed by a one-way ANOVA with Tukey's post hoc test. The experiment was independently performed three times with similar results.



at 14 days after infusion revealed that, while DOT cells were abundant in the blood, blood-rich organs and tumor lesions, they were virtually absent in healthy gut tissues (Fig. 2b).

Next, to evaluate the antitumor activity of DOT cells in CRC progression in vivo, we administered 10^7 DOT cells i.v. weekly, starting at 7 days after tumor inoculation, upon confirmation of

tumor establishment by luciferase signal detection and monitored tumor infiltration over time (Fig. 2c). Bioimaging follow-up clearly demonstrated the capacity of DOT cells to control tumor growth in vivo (Fig. 2d). These data constitute a preclinical proof of principle for using DOT cells in adoptive cell therapy of CRC as a first solid cancer indication.

Fig. 4 | NKG2D mediates CRC targeting by DOT cells. **a**, Flow cytometry histograms of NKR ligand expression in different CRC cell lines. **b**, Correlation of geometric mean of the mean fluorescence intensity of NKR ligand(s) on different CRC lines and targeting by DOT cells, assessed by the increase in the percentage of annexin V⁺ tumor cells upon incubation with DOT cells. Spearman's correlation coefficients (r) and P values are shown. Data are representative of three independent experiments. **c**, Analysis of NKG2D ligand expression, assessed by FPKM, in normal colon ($n = 41$ donors), primary colon cancer ($n = 453$ donors) and AML ($n = 151$ donors) obtained from TCGA repository. Data are presented as the means \pm s.e.m. and were analyzed by a Kruskal–Wallis test with Dunn's multiple-comparisons test. **d**, Quantification by flow cytometry of CD69, CD107a and TNF expression on DOT cells after 48-h incubation with plate-bound MICA–Fc chimera ($n = 3$ DOT donors). Data were analyzed by a two-tailed unpaired t -test. **e**, SW620 tumor cell death assessed by flow cytometry over a 3-h killing assay,

performed with freshly thawed DOT cells and DOT cells prestimulated with plate-bound MICA–Fc chimera for 48 h ($n = 2$ DOT donors). Data were analyzed by a one-way ANOVA with Tukey's post hoc test. In **d**, **e**, data are one representative of three experiments. **f**, SW620 tumor cell death assessed by flow cytometry over a 3-h killing assay performed with DOT cells in the presence of anti-NKG2D and anti-DNAM1 blocking antibodies or their isotype controls. Lines connect individual DOT donors ($n = 7$ DOT donors, pool of seven assays). Data were analyzed by a repeated-measures one-way ANOVA with Tukey's post hoc test. **g**, SW620 tumor cell death assessed by flow cytometry over a 3-h killing assay performed with control or *KLRK1*-knockout DOT cells. Data are presented as the means of the technical replicates of $n = 2$ independent experiments and were analyzed by a one-way ANOVA with Tukey's post hoc test. Data in **c**, **d** and **g** are presented as the means \pm s.e.m. Data in **e** are presented as the means.

DOT cells exhibit limited cytotoxicity in CRC tumors in vivo

Solid tumors often present as immunosuppressive environments²¹. Following our observation of efficient DOT cell homing to CRC, we assessed whether their functions were impacted by the TME. We conducted an extensive phenotypic and functional analysis of DOT cells before and 2 weeks after infusion into mice bearing established orthotopic CRC tumors, comparing both circulating and tumor-infiltrating DOT cells (Fig. 3a). The proportion of V δ 1⁺ DOT cells (among total human CD45⁺ cells) was around 80% in both the blood and the tumors, suggesting that the minor non V δ 1⁺ γ δ T cell subsets present in the DOT cell product are also recruited to the CRC tumors (Fig. 3b). Interestingly, we observed substantial alterations in the inhibitory and cytotoxic receptor repertoire of DOT cells in vivo. After in vitro expansion and differentiation of DOT cells in vitro (that is, before their infusion), TIM3 and CD96/Tactile were highly expressed, whereas PD1, TIGIT and LAG3 were mostly absent (Fig. 3c and Extended Data Fig. 3a). Strikingly, TIGIT was upregulated in vivo in both circulating and tumor-infiltrating DOT cells, while PD1 upregulation was confined to TILs. PD1⁺TIGIT⁺ cells but not PD1⁺TIM3⁺ cells were enriched within the tumors. Conversely, the expression of CD96, which competes with TIGIT for the same ligands (PVR/CD155 and Nectin 2/CD122), was downregulated in vivo. LAG3 (very low) and TIM3 (high) expression was more stable between in vivo DOT cells before and after injection (Fig. 3c and Extended Data Fig. 3a).

This immune checkpoint regulation in DOT cells was associated with a compromised cytotoxic profile in CRC. On one hand, the expression of NKG2D and DNAM1 decreased in DOT TILs, which upregulated the activation marker CD69 (Fig. 3d and Extended Data Fig. 3a). On the other hand, the release of cytolytic granules, as measured by CD107a/LAMP1, granzyme B and perforin expression, as well as TNF and IFN γ production, were significantly reduced in tumor-infiltrating DOT cells activated with PMA and ionomycin (Fig. 3e and Extended Data Fig. 3b). These findings support the notion that DOT cells, activated in the CRC

microenvironment, develop a dysfunctional phenotype characterized by dysregulated checkpoint receptor expression and impaired cytotoxicity. Therefore, we hypothesized that enhancing cytotoxic receptor engagement or blocking immune checkpoint receptors could improve CRC targeting by DOT cells.

NKG2D mediates CRC targeting by DOT cells

Among the NKRs expressed by DOT cells (Extended Data Fig. 1), DNAM1 and Nkp30 were previously shown to be required for AML targeting by DOT cells¹⁶. To elucidate which NKRs are important for CRC recognition by DOT cells, we profiled the respective ligand expression across multiple CRC cell lines using flow cytometry. While DNAM1 (PVR and Nectin 2) and Nkp30 (B7-H6) ligands were highly expressed in all cell lines analyzed, the expression pattern of the different NKG2D ligands (MICA-B and ULBP1–ULBP6) varied (Fig. 4a). Interestingly, this variable expression of NKG2D ligands correlated with the extent of DOT cell killing of the corresponding cell lines (Fig. 4b). Moreover, analysis of The Cancer Gene Atlas (TCGA) data showed an increased expression of genes encoding NKG2D ligands (especially *ULBP3* and *ULBP6*, followed by *ULBP1* and *ULBP2*) (Fig. 4c) and genes encoding DNAM1 and Nkp30 ligands (Extended Data Fig. 4a) in primary colon cancer compared to healthy colon samples or to AML samples.

To directly test the role of NKG2D in DOT cell function, we first used a gain-of-function approach through NKG2D crosslinking with plate-bound MICA–Fc chimera over 48 h. Decreased levels of membrane NKG2D reflected effective ligand engagement (Extended Data Fig. 5a) and were associated with enhanced DOT cell activation and a cytotoxic profile (Fig. 4d), ultimately leading to increased killing of CRC cells (Fig. 4e). Conversely, in loss-of-function experiments using anti-NKG2D blocking antibodies, we found reduced DOT cell killing of SW620 cells (Fig. 4f). DNAM1 blockade alone only moderately limited CRC targeting but, in combination with NKG2D blockade, further

Fig. 5 | Butyrate upregulates NKG2D ligand expression and increases CRC targeting by DOT cells.

a, Heat maps represent NKR ligand upregulation, assessed by flow cytometry in CRC upon 24-h exposure to different molecules. The fold change (FC) of expression over control with medium is represented. Data are representative of three independent experiments. **b**, The 3-h killing assays against CRC cell lines with or without treating cell lines with butyrate for 24 h ($n = 5$ donors, pool of three experiments). Data were analyzed by a one-way ANOVA with Tukey's post hoc test. **c**, NKG2D ligand upregulation, assessed by flow cytometry, in primary tumor specimens from participants with CRC upon butyrate exposure for 24 h, represented as the FC of control. **d**, The 24-h killing assay against primary CRC specimens with or without treating tumor cells with butyrate for 24 h. Lines connect values from the same participants ($n = 6$ participants, pool of four independent assays). **e**, **f**, Viability of DOT cells (**e**) and expression of NKG2D, DNAM1 and TNF (**f**), assessed by flow cytometry, upon exposure to different concentrations of butyrate for 3 h. In **e** and **f**, lines connect values from the same DOT donors ($n = 3$ donors). Data are one representative of two independent experiments. Data in **d**–**f** were analyzed by a repeated-

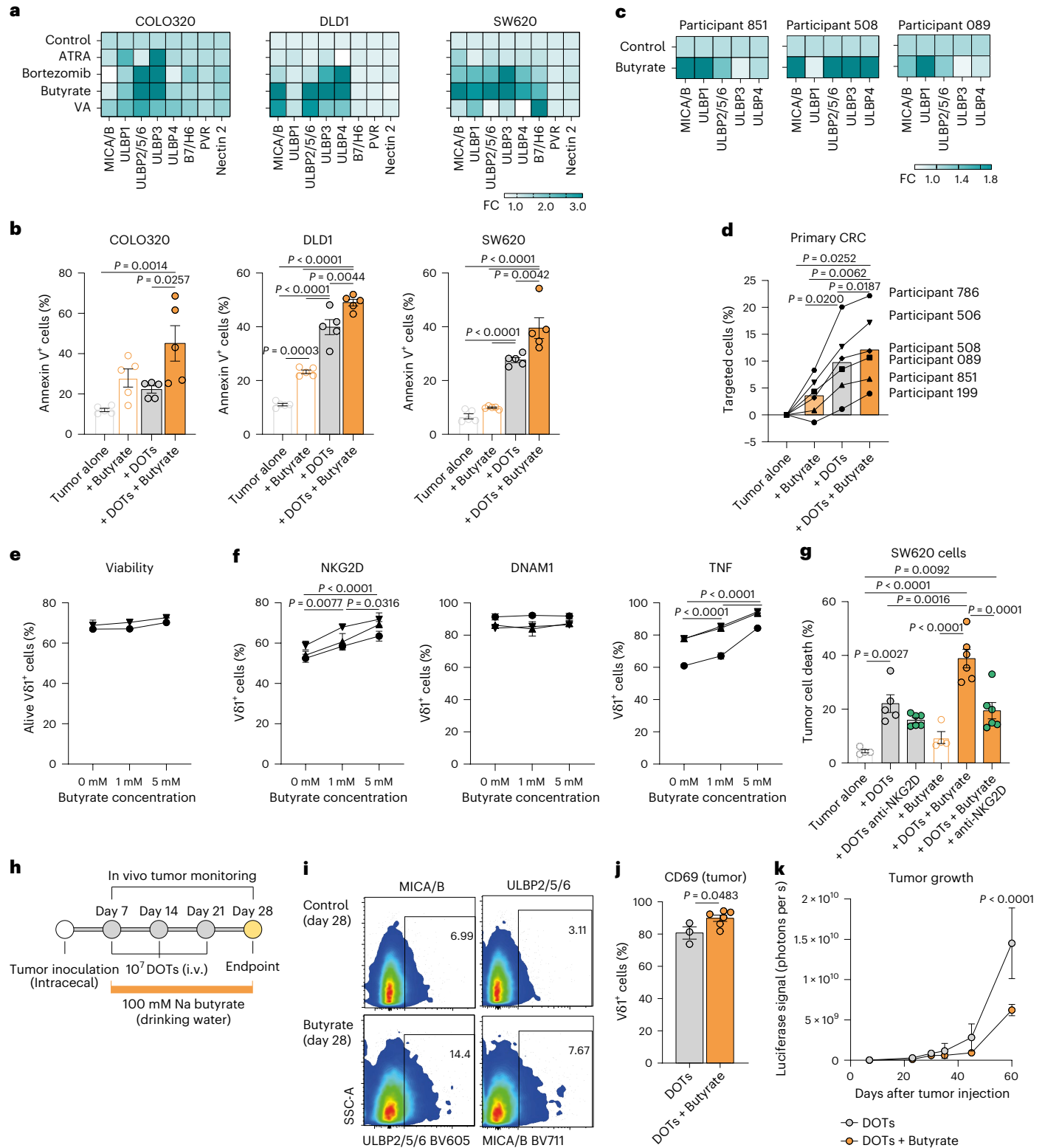
measures one-way ANOVA with Tukey's post hoc test. **g**, The 3-h killing assay of SW620 with or without butyrate pretreatment and/or anti-NKG2D blocking antibodies ($n = 3$ replicates of tumor alone \pm butyrate, $n = 6$ DOT donors). Data are one representative of three independent experiments and were analyzed by a one-way ANOVA with Tukey's post hoc test. **h**, Schematic representation of the administration of 100 mM sodium butyrate in drinking water of intracecal SW620 tumor-bearing mice and DOT cell i.v. treatment. **i**, Representative in vivo NKG2D ligand expression in the tumor (gated on alive human Epcam⁺ tumor cells) of control or butyrate-treated mice on day 28 after tumor inoculation, with percentages shown. **j**, CD69 expression, assessed by flow cytometry, on tumor-infiltrating DOT cells in butyrate-treated ($n = 6$ mice) and control mice ($n = 3$ mice). Data are one representative of two independent experiments and were analyzed by an unpaired t -test. **k**, Kinetics of intracecal SW620 tumor growth measured by luciferase signal using in vivo imaging of mice treated as depicted in **h** ($n = 6$ mice per group). Data are presented as the means \pm s.e.m. (pool of two independent experiments) and were analyzed by a repeated-measures two-way ANOVA with Sidák's multiple-comparisons test.

suppressed tumor killing by DOT cells (Fig. 4f). These data indicate a dominant role of NKG2D and a milder role of DNAM1 for the CRC targeting by DOT cells. Of note, neither Nkp30 blockade nor T cell receptor (TCR) blockade impaired CRC targeting by DOT cells (Extended Data Fig. 5b). To unequivocally demonstrate the importance of NKG2D in this process, we generated *KLRK1*-knockout (the gene encoding NKG2D) DOT cells using CRISPR–Cas9 technology, which resulted in the loss of NKG2D without compromising the expression of other receptors (Extended Data Fig. 5c). In agreement with the anti-NKG2D antibody

blockade results, NKG2D-deficient DOT cells exhibited impaired killing of SW620 cells (Fig. 4g), thus affirming the pivotal role of NKG2D in CRC targeting by DOT cells.

Butyrate improves NKG2D-mediated CRC targeting by DOT cells

We next postulated that enhancing NKG2D ligand recognition could improve DOT cell cytotoxicity against CRC. Hence, we screened molecules known to induce upregulation of NKG2D ligands²², focusing on



those with potential relevance in the CRC context, such as commensal bacterial metabolites, gut bioavailable molecules and chemotherapy agents. Among such candidates, butyrate, a short-chain fatty acid (SCFA) derived from the gut microbiota, achieved the highest and most consistent upregulation of multiple NKG2D ligands across different CRC cell lines (Fig. 5a). Building on these data, we pretreated CRC cells with butyrate for 24 h and then performed 3-h killing assays with DOT cells (also in the presence of butyrate). Consistent with the reported intrinsic butyrate cytotoxicity against CRC²³, 24-h exposure to 1 mM butyrate induced some tumor cell death. Nonetheless, preincubation with butyrate clearly increased the susceptibility of CRC lines to targeting by DOT cells (Fig. 5b). Even after washing out the medium and conducting killing assays in the absence of butyrate, CRC cell lines pretreated with butyrate maintained upregulated NKG2D ligands for the duration of the killing assay (Extended Data Fig. 6a), resulting in sustained increased targeting by DOT cells (Extended Data Fig. 6b). Consistent with the cell line data, NKG2D ligand expression was also enhanced in participant-derived CRC specimens following 24-h incubation with butyrate (Fig. 5c), leading to increased tumor targeting by DOT cells (Fig. 5d).

Considering that butyrate has also been described as an immunomodulatory molecule for effector T cells²⁴, we questioned its impact on DOT cell functions. Butyrate was not toxic for DOT cells, as their viability was preserved upon exposure to the concentrations used in the killing assays (Fig. 5e). In addition to enhancing NKG2D ligand expression on CRC cells, butyrate upregulated NKG2D (but not DNAM1) and TNF expression in DOT cells in a dose-dependent manner (Fig. 5f), without inducing other major changes in receptor repertoire (Extended Data Fig. 7a). Notably, while NKG2D levels on DOT cells decreased when cocultured with SW620 cells, this effect was more pronounced when the tumor cells were exposed to butyrate, suggesting increased NKG2D–NKG2D ligand interactions (Extended Data Fig. 7b). Importantly, we established that the butyrate-induced increase in CRC targeting is mediated by NKG2D as it was fully reversed upon blockade of this receptor (Fig. 5g).

To translate these findings *in vivo*, we administered sodium butyrate in the drinking water from the initiation of DOT cell treatment in the SW620 orthotopic xenograft model (Fig. 5h). As predicted, increased butyrate levels in the cecum (Extended Data Fig. 8a) upregulated NKG2D ligands in the CRC tumors of mice treated with butyrate (Fig. 5i), without showing signs of toxicity (Extended Data Fig. 8b,c). Even though the percentage and numbers of tumor-infiltrating DOT cells remained unchanged (Extended Data Fig. 8d,e), they showed heightened activation, as indicated by increased CD69 expression (Fig. 5j) and led to delayed tumor growth in mice treated with butyrate compared to controls (Fig. 5k). Thus, butyrate treatment enhances NKG2D-mediated recognition of CRC and improves tumor control *in vitro* and *in vivo*.

Blockade of PD1 and TIGIT enhances DOT cell efficacy

In addition to boosting NKG2D activation, we hypothesized that blocking immune checkpoints (Fig. 3) could maximize the anti-CRC functions of DOT cells. Among the checkpoint receptors under study, TIGIT and PD1 were clearly the most upregulated on DOT cells *in vivo* (Extended Data Fig. 9a), defining a population of tumor-infiltrating PD1⁺TIGIT⁺ DOT cells (Fig. 3c), which prompted us to investigate their impact on DOT cell activities. Compared to their PD1[−]TIGIT[−] counterparts, tumor-infiltrating PD1⁺TIGIT⁺ DOT cells coexpressed higher levels of TIM3 while maintaining similar levels of NKG2D and DNAM1 (Fig. 6a). The expression of these checkpoint receptors has been linked to activation rather than terminal exhaustion of Vδ1⁺ T cells, whose cytotoxic potential could be further enhanced through checkpoint blockade^{4,8,25}. In alignment, we found PD1⁺TIGIT⁺ DOT cells to express higher levels of effector molecules, including CD107a, granzyme B and IFN γ , after stimulation with PMA and ionomycin (Fig. 6b).

It is well established that tumor cells upregulate inhibitory ligands in response to inflammatory cues of the TME such as IFN γ , which represents an immune evasion mechanism²⁶. Given the significant secretion of IFN γ by DOT cells (Extended Data Fig. 1c) and particularly by intratumoral PD1⁺TIGIT⁺ DOT cells, we conjectured that they might induce the expression of PD1 and TIGIT ligands on tumor cells, potentially dampening DOT cell cytotoxicity. Consistent with this hypothesis, we observed that IFN γ exposure increased the levels of surface PDL1 and PVR (PD1 and TIGIT ligands, respectively) on SW620 cells without altering Nectin 2 or NKG2D ligands (Extended Data Fig. 9b). Moreover, we demonstrated that the presence of DOT cells also triggers PDL1 expression on SW620 cells in an IFN γ -dependent manner because neutralization of DOT cell-derived IFN γ prevented PDL1 expression *in vitro* (Fig. 6c). Interestingly, IFN γ -induced PDL1-expressing SW620 cells also exhibited heightened levels of PVR (Fig. 6d), which might provide negative feedback on PD1⁺TIGIT⁺ DOT cells *in vivo*.

In turn, to assess how PD1 and TIGIT might affect DOT cell cytotoxicity, we cultured DOT cells for 24 h in the presence of plate-bound PDL1 and PVR. While DNAM1, CD96 and TIGIT compete for binding to PVR, their relative expression levels in DOT cells (typically with low TIGIT expression) are finely tuned to maintain cytotoxicity. However, the increased levels of TIGIT and decreased levels of DNAM1 and CD96 observed in the CRC context (as depicted in Fig. 3) could tip the balance toward an inhibitory function of PVR through TIGIT engagement. In CD8⁺ $\alpha\beta$ T cells, PD1 and TIGIT converge to inhibit DNAM1-mediated costimulation, with TIGIT competing for its ligand and PD1 inhibiting DNAM1 phosphorylation²⁷. In the absence of additional stimulation (in addition to IL-15), single binding to PVR or PDL1 minimally impacted DOT cell cytotoxicity. However, mutual engagement with PVR and PDL1 markedly reduced granzyme B and perforin production, confirming that PDL1 interferes with PVR–DNAM1 activation. When DNAM1 and CD96 were blocked, favoring PVR binding to TIGIT, PVR alone dampened granzyme B and perforin production without any additional effect of PDL1 (Fig. 6e). Additionally, engagement with PVR and PDL1 also diminished NKG2D expression (Extended Data Fig. 9c), thereby affecting not only DNAM1-mediated activation but also NKG2D-mediated activation. These findings suggest that PD1 and TIGIT collaborate to suppress distinct activation mechanisms and ultimately impair DOT cell cytotoxicity.

In alignment, while the individual blockade of either PD1 or TIGIT produced minor effects, their combination led to significant increases in *in vitro* killing of SW620 cells (Fig. 7a) and primary CRC samples (Fig. 7b). Lastly, to evaluate the impact of checkpoint blockade *in vivo*, we designed a therapeutic approach wherein clinical-grade blocking antibodies targeting TIGIT (vibostolimab) and/or PD1 (nivolumab) were administered intraperitoneally (i.p.) weekly concurrently with DOT cell infusions in orthotopic CRC-bearing mice (Fig. 7c). Effective blockade was confirmed by epitope masking and decreased PD1 and TIGIT staining in circulating and tumor-infiltrating DOT cells at day 28 after tumor inoculation (Fig. 7d and Extended Data Fig. 9d). In agreement with the *in vitro* data, the combination of anti-PD1 and anti-TIGIT treatment maximized (compared to controls and monotherapies) DOT cell functions, especially degranulation of cytotoxic granules (CD107a) and granzyme B and TNF expression (Fig. 7e). Most importantly, the coadministration of anti-PD1 and anti-TIGIT resulted in the most striking tumor control observed in this study (Fig. 7f), thus supporting the application of dual PD1–TIGIT checkpoint blockade in combination with adoptive DOT cell transfer for CRC treatment.

Imbalanced receptor repertoire of Vδ1⁺ TILs in participants with CRC

To assess whether the TME had a similar impact (as observed for adoptively transferred DOT cells in our xenograft model) on endogenous Vδ1⁺ T cells from participants with CRC, we conducted multicolor spectral flow cytometry on matched tumor and blood samples from

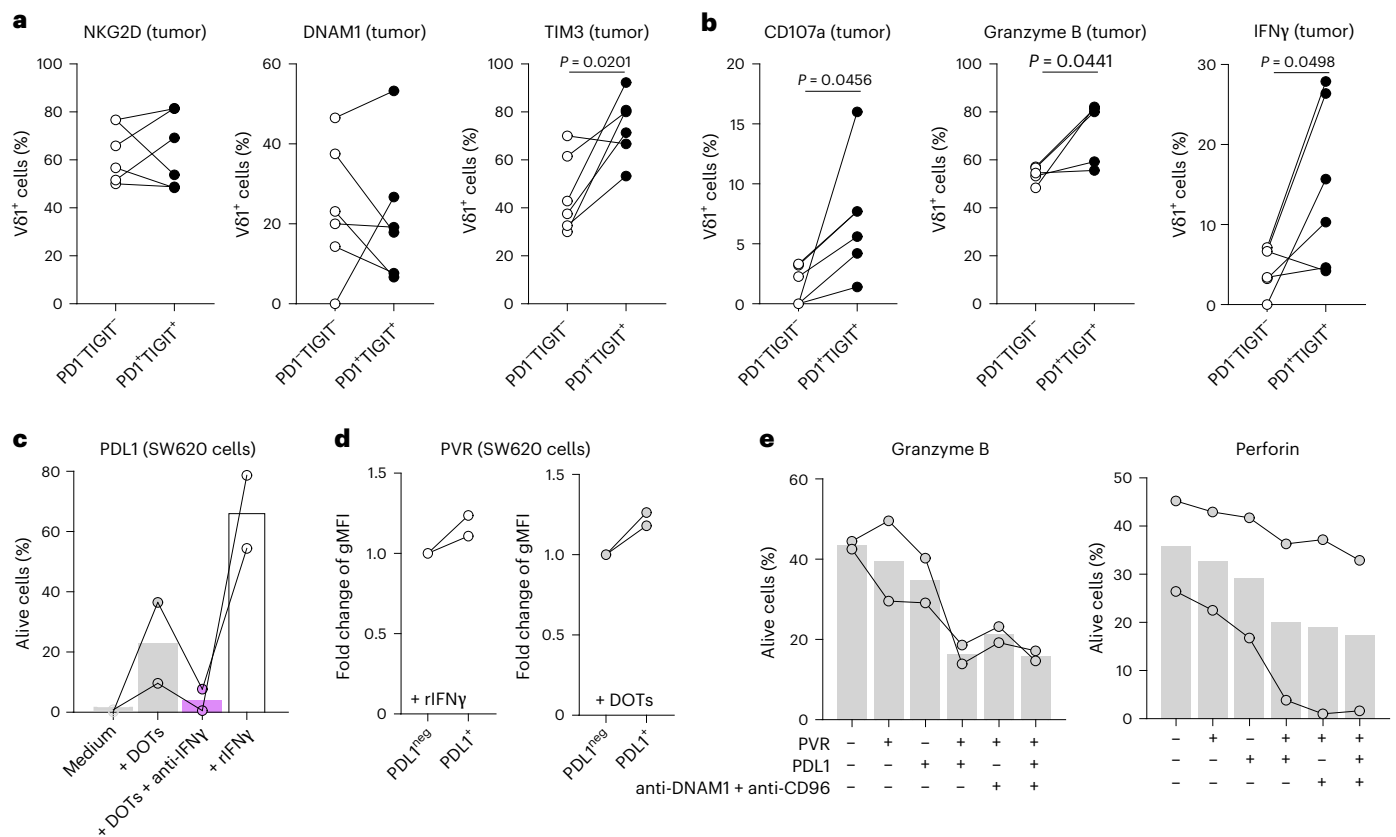


Fig. 6 | PD1 and TIGIT engagement synergistically inhibit DOT cell function.

a, Expression of NKG2D, DNAM1 or TIM3 in PD1⁺TIGIT⁻ and PD1⁺TIGIT⁺ DOT cells in tumors from xenografted mice ($n = 5$ mice). **b**, Expression of CD107a, granzyme B, IFN γ and TNF in PD1⁺TIGIT⁻ and PD1⁺TIGIT⁺ DOT cells in tumors after 3 h of PMA and ionomycin stimulation ($n = 6$ mice). In **a** and **b**, data points from the same mice are connected by lines and were analyzed by a two-tailed paired t -test. The experiment was performed three times, with similar results. **c**, PDL1 expression on SW620 cells upon 24-h incubation with either rIFN γ DOT cells or DOT cells and neutralizing anti-IFN γ antibody, measured by flow cytometry (the means of the technical replicates of $n = 2$ independent experiments are presented).

Data are presented as the means \pm s.e.m. and were analyzed by a one-way ANOVA with Tukey's post hoc test. **d**, Geometric mean fluorescence intensity of PVR levels in PDL1⁻ and PDL1⁺ SW620 cells upon IFN γ or DOT cell exposure (the means of the technical replicates of $n = 2$ independent experiments are presented), measured by flow cytometry and analyzed by a two-tailed paired t -test. **e**, Percentage of DOT cells expressing granzyme B and perforin after 24-h incubation with plate-bound PVR and/or PDL1 in the presence or not of anti-DNAM1 and anti-CD96 blocking antibodies (the means of the technical replicates of $n = 2$ independent experiments are presented).

participants with CRC, as well as blood from healthy controls. Unsupervised hierarchical analysis divided naturally existing V δ 1⁺ T cells into nine distinct clusters on the basis of the expression of inhibitory and cytotoxic receptors (Fig. 8a). Whereas similar clusters classified blood V δ 1⁺ T cells from both participants and healthy controls, clusters 7, 8 and 9 were notably enriched in tumor-infiltrating V δ 1⁺ T cells (Fig. 8b). These clusters, characterized by high PD1 expression, also coexpressed TIGIT. Additionally, these PD1⁺TIGIT⁺ tumor-specific clusters exhibited intermediate levels of NKG2D and CD96, with low levels of KLRG1 (Fig. 8c). Among them, cluster 8 expressed the heterodimer NKG2A-CD94, while cluster 9 was defined by CD158 (KIR2DL1/S1/S3/S5) and CD69 expression, with low DNAM1 levels. We then quantified the abundance of V δ 1⁺ T cells expressing these receptors among the different groups analyzed, confirming that PD1⁺TIGIT⁺ cells were enriched in the tumors. Similar to infused DOT cells, TIGIT was highly expressed in both circulating and tumor-infiltrating V δ 1⁺ T cells, whereas PD1 expression was restricted to TILs (Fig. 8d) and PD1⁺TIGIT⁺ cells coexpressed high TIM3 levels (Extended Data Fig. 10a). Outside of KLRG1 being highly expressed in circulating cells from participants and controls and decreased in tumors, the expression of the remaining inhibitory receptors evaluated showed no significant differences among the groups (Extended Data Fig. 10b). Expression of the natural cytotoxicity receptors Nkp30, Nkp44 and Nkp46 was restricted to the V δ 1⁺ TILs of a few individuals (Extended Data Fig. 10b). In contrast, NKG2D and DNAM1

were substantially expressed in blood V δ 1⁺ T cells and downregulated in CRC tumors, with NKG2D⁺DNAM1⁺ cells significantly decreased in both circulating and TILs from participants with CRC (Fig. 8d).

In conclusion, these findings reveal a parallel dysregulation of cytotoxic and inhibitory receptors in both endogenous V δ 1⁺ T cells and adoptively transferred DOT cells, potentially impairing their antitumor functions in the CRC. This suggests that insights gained from studying DOT cells in vivo may be applicable to the clinical setting and the strategies developed to enhance DOT cell efficacy in preclinical models may hold promise for bolstering endogenous V δ 1⁺ T cell cytotoxicity in persons with CRC.

Discussion

DOT cells are the result of an established clinical-grade V δ 1⁺ $\gamma\delta$ T cell-based protocol for adoptive cell therapy^{12,14,16,17}. While all previous research and development progress was made in the context of hematological malignancies¹⁴⁻¹⁷, leading to an ongoing clinical trial in AML (NCT05886491), the current study positions DOT cells for immunotherapy of solid tumors, particularly CRC.

The choice of CRC for a first proof of concept for DOT cells in solid cancers was based on a combination of multiple factors. First, V δ 1⁺ $\gamma\delta$ T cells have been known for three decades to be a prevalent TIL population in CRC^{28,29}. Second, V δ 1⁺ $\gamma\delta$ TILs or PBLs showed anti-CRC cytolytic potential ex vivo⁴, in vitro^{3,29} and in vivo¹¹ following restimulation. Third,

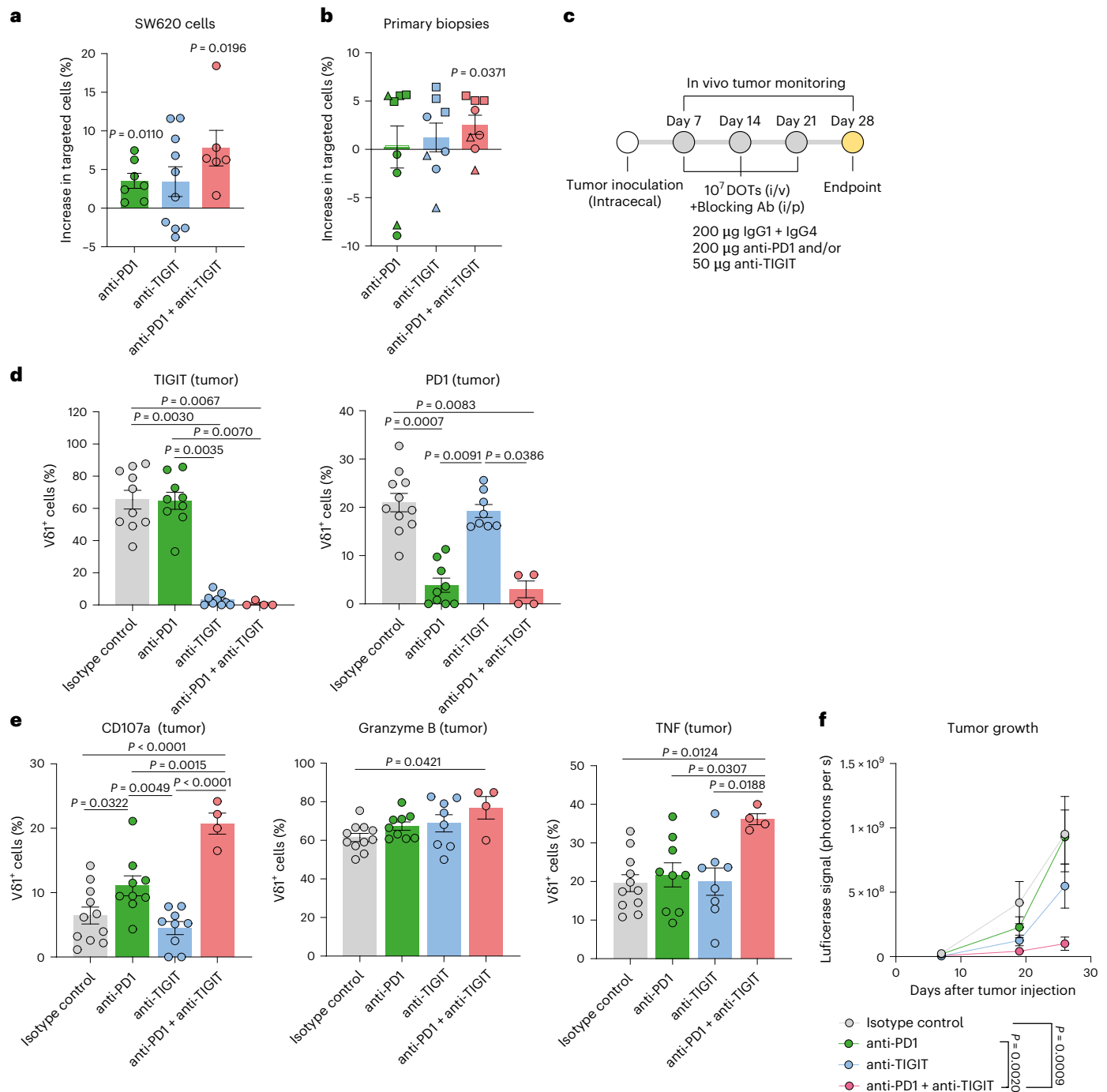


Fig. 7 | Blockade of TIGIT and PD1 receptors enhances DOT cell cytotoxicity against CRC. **a**, Increase in the percentage of SW620 tumor cell death, assessed by annexin V flow cytometry staining, upon 3-h in vitro incubation with DOT cells in the presence anti-PD1 ($n = 7$ DOT donors), anti-TIGIT ($n = 10$ DOT donors) or anti-PD1 + anti-TIGIT ($n = 6$ DOT donors) in comparison to isotype controls. Data are presented as the means \pm s.e.m. (pool of 11 different assays) and were analyzed by a two-tailed one-sample t -test against a hypothetical value of 1. **b**, Increase in the percentage of primary tumor cell death (obtained from CD45-depleted CRC primary specimens), assessed by caspase 3/7 flow cytometry staining, upon 24-h in vitro incubation with DOT cells in the presence of blocking antibodies against different checkpoints in comparison to isotype controls. Different symbols represent different participant-derived specimens ($n = 8$ specimens). Data were analyzed by a two-tailed one-sample t -test against a hypothetical value of 1 (data pooled from three assays). **c**, Schematic representation of the in vivo (i.p.) administration of ICB (or isotype control) antibodies concomitant with DOT cell infusions (at days 7, 14 and 21 after tumor inoculation) in the intracerecal SW620

model. **d**, Quantification of TIGIT and PD1 expression on tumor-infiltrating V δ 1⁺ cells at day 28 after tumor injection upon in vivo checkpoint blockade (gated on alive human CD45⁺CD3⁺TCRV δ 1⁺ cells) ($n = 11$ control, $n = 9$ anti-PD1, $n = 8$ anti-TIGIT and $n = 4$ anti-PD1 + anti-TIGIT mice). Data were analyzed by a Kruskal–Wallis test with Dunn’s multiple-comparisons test. **e**, Flow cytometry quantification of CD107a, granzyme B and TNF in tumor-infiltrating DOT cells after checkpoint blockade therapy in vivo and after 3 h of PMA and ionomycin stimulation and protein translocation inhibitors ($n = 11$ control, $n = 9$ anti-PD1, $n = 8$ anti-TIGIT and $n = 4$ anti-PD1 + anti-TIGIT mice). Data were analyzed by a one-way ANOVA with Tukey’s post hoc test. **f**, Intracerecal SW620 tumor growth upon DOT cell treatment and checkpoint blockade, measured by luciferase signal using in vivo imaging ($n = 12$ control, $n = 10$ anti-PD1, $n = 10$ anti-TIGIT and $n = 8$ anti-PD1 + anti-TIGIT). Data in **d–f** were pooled from two independent experiments and analyzed by a repeated-measures two-way ANOVA with Tukey’s multiple-comparisons test. Differences between the different groups on day 28 are indicated. Data are presented as the means \pm s.e.m.

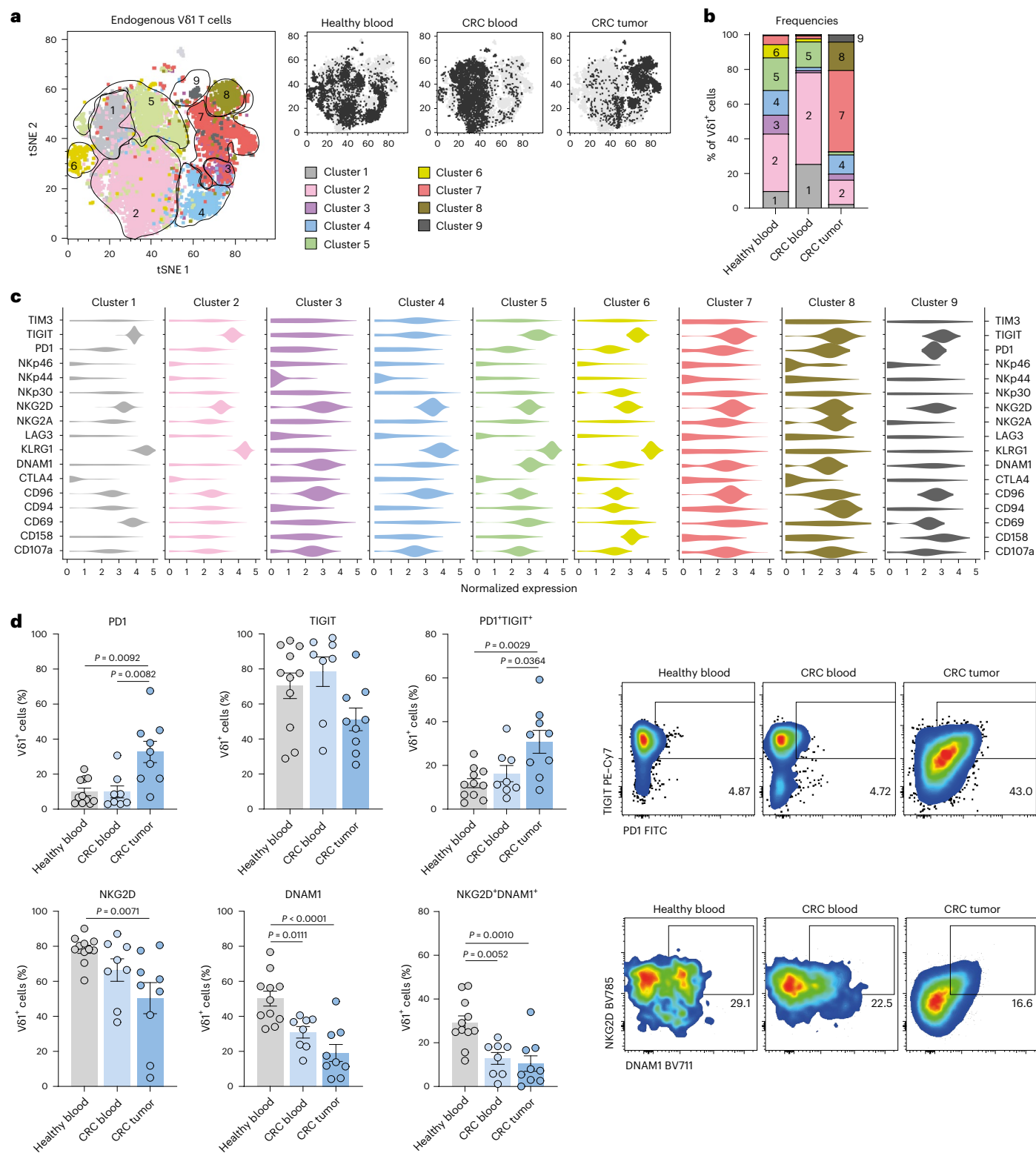


Fig. 8 | Endogenous V δ 1⁺ T cells exhibit a dysregulation of checkpoint and cytotoxic receptors in CRC tumors. a, The *t*-distributed stochastic neighbor (tSNE) embedding plot of V δ 1⁺ cells isolated from blood and tumors from participants with CRC and blood samples from healthy donors, considering the expression levels of NKRs, natural cytotoxicity receptors and inhibitory receptors measured by spectral flow cytometry. A stochastic pool of six samples per group was used. Left, colors represent the nine clusters automatically identified after considering the parameters evaluated. Right, the distribution of cells throughout the clusters according to their origin. **b**, Frequencies of

the different clusters of V δ 1⁺ cells among each group; each cluster is depicted with the same colors as in **a**. **c**, Violin plots show the normalized expression of each marker along the different clusters. **d**, Quantification of expression and representative density plots of PD1–TIGIT and NKG2D–DNAM1, represented as the percentage of positive cells among alive V δ 1⁺ cells ($n = 11$ healthy blood samples, $n = 8$ CRC blood samples and $n = 9$ CRC tumor samples). Data were analyzed by a one-way ANOVA with Tukey's post hoc test. Data are presented as the means \pm s.e.m.

$\gamma\delta$ T cells have been associated with good prognosis in large cohorts of persons with CRC²¹⁰. Fourth, V δ 1⁺ $\gamma\delta$ T cells were recently identified as important contributors to the responses to ICB in persons with mutant *B2M* CRC⁴. Interestingly, this latter study found V δ 1⁺ TILs to express and use NKRrs, especially NKG2D, highlighting the potential of using DOT cells as adoptive cell therapy given their heightened expression of NKG2D, among other NKRrs¹⁴.

Recent reports from phase 2 clinical trials demonstrated near 100% responses to neoadjuvant ICB in persons with locally advanced MSI CRC. However, responses to ICB by persons with MSS CRC, accounting for most CRC cases, are extremely rare in metastatic settings, reiterating the need for novel approaches^{30,31}. We now provide evidence for a strong and broad reactivity of DOT cells against both MSI and MSS CRC cell lines, as well as PDOs, in vitro. This breath of CRC targeting may be accounted by innate sensing through NKG2D, as its CRISPR-mediated deletion on DOT cells impaired CRC targeting and the expression of NKG2D ligands correlated with the extent of DOT cell killing. DNAM1 blockade (and not NKp30) showed a substantial effect only when NKG2D was neutralized, suggesting a hierarchical contribution of these two receptors to CRC targeting. This is particularly interesting because our previous studies on AML identified DNAM1 and NKp30 ligands but not NKG2D ligands as the key mediators of DOT cell recognition^{16,17}. Consistent with the preferential role of NKG2D in CRC (versus AML) recognition by DOT cells, our analysis of TCGA data showed increased expression of genes encoding NKG2D ligands in primary colon cancer compared to AML samples. Importantly, the expression of genes encoding NKG2D ligands was also higher in CRC than in healthy colon samples, which provides a mechanism for discrimination of malignant versus normal gut tissue. In fact, our in vivo model showed a preferential homing of DOT cells to CRC lesions than to neighboring healthy gut tissues.

Notwithstanding the augmented expression of NKG2D ligands on many CRC primary samples or cell lines, we observed an intrinsic variability that led us to devise a strategy to boost DOT cell activity through upregulation of NKG2D ligands. Upon screening molecules known to induce such upregulation²², the SCFA butyrate, one of the most important metabolites produced by commensal gut microbiota, produced the highest and most consistent upregulation of multiple NKG2D ligands and its administration (in the drinking water) resulted in reduced tumor burden in vivo. These results are in line with the reported increased cytotoxic response of CD8⁺ T cells mediated by butyrate in murine CRC models through the promotion of IL-12 signaling²⁴. These and other results, such as the increased butyrate levels in the serum of persons with cancer that respond to chemotherapy²⁴, have fueled the enthusiasm on the development of therapeutic strategies to boost butyrate levels, especially in CRC, because of its anatomic proximity to commensal microbiota. In particular, *Clostridium butyricum*, a butyrogenic gut symbiont has been largely suggested as a potential therapeutic intervention for CRC^{32,33}. Our data underscore the potential for exploring the levels of bioavailable butyrate as a biomarker for clinical response to DOT cell therapy.

Another striking observation in our CRC xenograft model was the upregulation of the immune checkpoints TIGIT and PD1 in tumor-infiltrating DOT cells. Even though these PD1⁺TIGIT⁺ DOT cells exhibit enhanced cytotoxic markers, the overall DOT cell cytotoxic profile was compromised in tumors. Similarly, unsupervised analyses identified a significant fraction of V δ 1⁺ TILs from participants with CRC coexpressing both PD1 and TIGIT, which are increased in tumors when compared to their circulating counterparts. These results imply a comparable imbalance of effector and cytotoxicity versus inhibitory receptors in both endogenous V δ 1⁺ TILs and DOT cells, likely compromising their overall ability to combat tumors. The expression and function of PD1 on V δ 1⁺ T cells has been the focus of various recent reports. Their overwhelming conclusion is that, in contrast with CD8⁺ T cells, V δ 1⁺ T cells expressing PD1 are not 'functionally exhausted' but instead

show hallmarks of activation and effector molecules^{4,8,25,34}. Moreover, when tested against CRC cell lines or organoids, fluorescence-activated cell-sorted and expanded PD1⁺ $\gamma\delta$ T cells, which mostly contained V δ 1⁺ (and to a lesser extent V δ 3⁺) T cells, displayed increased cytotoxic potential compared to PD1⁻ $\gamma\delta$ T cells⁴. Not only in CRC⁴ but also in renal cell²⁵ and Merkel cell carcinoma³⁵, as well as in well-controlled in vitro assays in the presence of recombinant (r)PD1 (ref. 8), these 'activated' V δ 1⁺ T cells were unleashed (in terms of antitumor cytotoxicity and cytokine production and degranulation) upon anti-PD1 ICB.

Unexpectedly, we found anti-PD1 ICB (alone) to provide very little benefit to adoptive DOT cell therapy. Instead, we observed a marked synergy between TIGIT and PD1 blockade both in vitro and, most strikingly, in vivo. In fact, TIGIT was the most upregulated immune checkpoint on DOT cells upon infusion in our CRC xenograft model. In concordance with previous observations^{25,36} these TIGIT⁺ cells still bore cytotoxic potential as observed by their restored cytotoxic function upon checkpoint blockade. Importantly, TIGIT expression was previously noted as very high on V δ 1⁺ TILs^{25,35,36}, which we also now confirm in circulating V δ 1⁺ T cells from persons with CRC, suggesting not only that the expression levels that we observed in our in vivo model are physiological but also that V δ 1⁺ T cells in individuals with cancer may bear cytotoxic potential if their response is properly unleashed.

Recent work on human CD8⁺ T cells highlighted a cooperation between PD1 and TIGIT in promoting suppression and exhaustion. On the one hand, stem-like PD1⁺TIGIT⁺ progenitors are committed to the generation of dysfunctional memory cells³⁷. On the other hand, TIGIT–PD1 synergy in ICB indicated that both PD1 and TIGIT converge to negatively regulate DNAM1 costimulation²⁷. While TIGIT limits DNAM1 costimulation by competing for their common ligand PVR, PD1 inhibits phosphorylation of both DNAM1 and CD28 through its immunoreceptor tyrosine-based inhibitory motif-containing intracellular domain. Thus, maximal antitumor CD8⁺ T cell responses require blockade of both TIGIT and PD1, arguing for combinatorial targeting in the clinic²⁷. In agreement, we found that engagement of both PD1 and TIGIT is required to reduce granzyme B and perforin in DOT cells while also reducing NKG2D expression. Of note, a phase 2 clinical trial showed improvement in overall response rate and progression-free survival in persons with nonsmall cell lung cancer who received a combination of anti-PD1 and anti-TIGIT antibodies³⁸. Our data here show that the same principle applies to DOT cells in preclinical models of CRC.

Altogether, this study paves the way for testing DOT cell-based products in combinatorial approaches for CRC while provoking further research in other solid cancers for which immunotherapy is yet to provide substantial clinical benefit.

Methods

Ethical statement

This investigator-initiated study was conducted in accordance with the principles of the Declaration of Helsinki and the International Conference on Harmonization Good Clinical Practice guidelines and was approved by the ethics committee of Centro Académico de Medicina de Lisboa (numbers 329/20 and 329/20/21A). All participants included in the study provided written informed consent before sample collection. Participants were not compensated for study participation. Mouse experiments performed in this study were evaluated and approved by our institutional ethical committee (iMM-Orbea) and the national competent authority (Direção-Geral de Alimentação e Veterinária) under the license number 0421/000/000/2023.

Participant samples

CRC tumor specimens from participants (42% women, aged 63 ± 11 years) were prospectively collected by colonoscopy and before treatment between January 2023 and March 2024 from the Hospital Santa Maria. In addition, a blood sample was collected from the same participants and peripheral blood mononuclear cells (PBMCs) were

cryopreserved at the biobank of the Gulbenkian Institute for Molecular Medicine. In parallel, blood samples from 11 randomized sex-matched and age-matched healthy donors from the biobank were analyzed. All individuals included in this study provided informed consent and the study was approved by the institutional ethics committee in accordance with the Declaration of Helsinki.

From dissection to processing, the tumor specimens were maintained in DMEM (Gibco) with 5% penicillin–streptomycin (Gibco), 5% fungizone–amphotericin B (Gibco), 0.2% gentamicin (Gibco) and 0.1% metronidazole (Duchefa Biochemie). Within the first 3 h after collection, tumor biopsies were cut into 1–2-mm³ pieces and cryopreserved in CryoStor CS10 cell cryopreservation medium (Merck) in liquid nitrogen until used. Tumor specimens were chosen randomly for the different assays performed.

Seven PDOs and tumor-infiltrating leukocytes, expanded from participants with CRC (four MMR-p/MSS and three MMR-d/MSI) at the Leiden University Medical Center as described below, were included in this work. Participant samples were anonymized and processed in compliance with the medical ethical guidelines outlined in the Code of Conduct for Proper Secondary Use of Human Tissue by the Dutch Federation of Biomedical Scientific Societies.

DOT cell expansions

DOT cells were generated as previously described, with minor modifications. PBMCs were isolated from buffy coats of healthy volunteers using Ficoll–Hypaque gradient centrifugation. Buffy coats were obtained from the Instituto Português do Sangue e da Transplantação with institutional approval. PBMCs were depleted of $\alpha\beta$ T cells by incubation with anti-TCR $\alpha\beta$ biotin, followed by anti-biotin microbeads and magnetic separation using LS columns (Miltenyi Biotec). DOT cells were derived from $\alpha\beta$ -depleted PBMCs cultured on the G-REX platform (Wilson Wolf Manufacturing) with OpTmizer-CTS medium, supplemented with 2.5% heat-inactivated human plasma, 2 mmol L⁻¹ L-glutamine, 50 U per ml penicillin and 50 μ g ml⁻¹ streptomycin. On day 0, cultures received rIL-4 (100 ng ml⁻¹), rIFN γ (70 ng ml⁻¹), rIL-21 (7 ng ml⁻¹), rIL-1 β (15 ng ml⁻¹) (all from PeproTech) and anti-CD3 (OKT3, 140 ng ml⁻¹; BioLegend). On day 7, rIL-21 (13 ng ml⁻¹), rIL-15 (70 ng ml⁻¹) and anti-CD3 (1 μ g ml⁻¹) were added. On day 11, fresh medium was added with rIL-15 (100 ng ml⁻¹) and anti-CD3 (1 μ g ml⁻¹). Cells were incubated at 37 °C, 5% CO₂. On day 14, DOT cells were harvested, cryopreserved in CryoStor (Merck) and stored in liquid nitrogen. Only expansions exceeding 65% V δ 1⁺ T cells were used.

CRC PDOs

PDOs were derived from both MMR-p/MSS and MMR-d/MSI CRC tumors through resection from the colon.

For the establishment of the respective organoids from tumor samples, tumor tissue was mechanically dissociated with collagenase D and DNase I (Roche) for 30 min at 37 °C. Cells were embedded in cold Matrigel reduced growth factor basement membrane extract type C2 (Corning). Drops of around 1 cm² of Matrigel containing tumor cells were placed on a prewarmed 12-well plate. Matrigel was solidified at 37 °C for 20 min. When solidified, CRC organoid medium (described below) was added to the plates to cover the Matrigel drops and plates were placed into the incubator. Organoids were passaged every 1–2 weeks on the basis of their growth rate by incubating them in TrypLE Express (Gibco) for 5–10 min before re-embedding in β -mercaptoethanol. To prevent microbial contamination, 1 \times Primocin (Invivogen) was added during the first 2 weeks of culture.

CRC organoid medium consisted of advanced DMEM/F12 (Gibco) supplemented with 2 mM ultraglutamine I (Lonza), 10 mM HEPES (Sigma), 100 U per ml penicillin and streptomycin (Gibco), 10% Noggin-conditioned medium (Peprotech), 20% R-spondin 1-conditioned medium (Peprotech), 1 \times B27 supplement without vitamin A (Gibco), 1.25 mM *N*-acetylcysteine (Sigma-Aldrich), 10 mM

nicotinamide (Sigma-Aldrich), 50 ng ml⁻¹ human rEGF (Peprotech) and 500 nM A83-01 (Tocris).

Mutations in hotspots across oncogenes and tumor suppressor genes were determined by making use of the molecular diagnostic pipeline at the Leiden University Medical Center (Department of Pathology) (Supplementary Table 1). The description of the cancer hotspot panel is available online (https://www.palga.nl/media/uploads/pdf/4/9/496_102-chpv6-lumc.pdf).

TIL expansions

TIL expansion was carried out by culturing CRC tumor fragments in a 24-well plate using complete IMDM, which included IMDM (Lonza BioWhittaker), 5% heat-inactivated pooled human serum (Sanquin), 100 IU per ml penicillin, 100 μ g ml⁻¹ streptomycin, 4 mM L-glutamine (Lonza BioWhittaker) and 1,000 IU per ml rIL-2 (Aldesleukin, Novartis). After 14–21 days, TILs were isolated and cryopreserved for future use. To increase T cell numbers before reactivity assays, a rapid expansion protocol was applied. TILs were cultured with rIL-2 (3,000 IU per ml), OKT3 (30 ng ml⁻¹; Miltenyi Biotec) and irradiated feeder cells (40 Gy, 100–200-fold excess) for 4–5 days. Feeder cells were PBMCs obtained from healthy donor blood provided by Sanquin. The culture was maintained for up to 2 weeks in T cell medium supplemented with rIL-2 (3,000 IU per ml).

In vitro killing assays

All CRC cell lines, COLO-320DM (CCL-220), DLD1 (CCL-221), HCT116 (CCL-247), HT29 (HTB-38), SW480 (CCL-228) and SW620 (CCL-227), were obtained from the American Type Culture Collection. Cell lines were grown in RPMI-1640 (Gibco) with 10% FBS and 1% penicillin–streptomycin with 5% CO₂ at 37 °C. For killing assays, trypsinized CRC cells were stained with CellTrace Violet (Thermo Fisher Scientific) in PBS and washed before being cocultured with DOT cells at a 5:1 ratio of effector to target for 3 h in the presence of 100 ng ml⁻¹ IL-15 (Peprotech). All killing assays were performed in RPMI-1640 (Gibco) with 10% FBS (Gibco), 1% HEPES (Gibco), 1% pyruvate (Gibco), 1% CTS Glutamax (Gibco), 1% MEM nonessential amino acids (Gibco) and 0.2% Mycozap (Lonza), hereafter referred to as complete RPMI. Cells were stained with annexin V (AlexaFluor 647, BioLegend) and analyzed in LSR Fortessa (BD Biosciences). Data were analyzed with FlowJo software (Tree Star).

For primary CRC specimens, samples were processed as described previously³⁹; cryopreserved tumor pieces were digested with liberase (Roche) and DNase I (Roche) in RPMI-1640 (Gibco) for 30 min at 37 °C with agitation. The preparations were passed through a 70- μ m filter with the help of a syringe piston and washed with RPMI-1640 with 10% FBS and 1% penicillin–streptomycin. Single-cell suspensions were stained with anti-human CD45 monoclonal antibody conjugated to biotin (clone 2B11, Invitrogen) for 10 min at 4 °C. After washing with PBS, cells were incubated with anti-biotin microbeads (Miltenyi Biotec) followed by magnetic depletion of CD45⁺ cells using LD columns (Miltenyi Biotec) following the manufacturer's instructions. Subsequently, CD45-depleted tumors were stained with CellTrace Violet (Thermo Fisher Scientific) and washed before coincubation with DOT cells at a 5:1 ratio of effector to target in complete RPMI in the presence of 100 ng ml⁻¹ IL-15 (Peprotech) for 24 h. Then, cells were stained with caspase 3/7 green (Invitrogen) and analyzed in Fortessa (BD Biosciences). Data were analyzed with FlowJo software (Tree Star).

For CRC PDOs, growing PDOs were dissociated using TrypLE Express (Gibco) for 10–15 min at 37 °C. Tumor cells were plated in a U-bottom 96-well plates in the presence or absence of autologous expanded TILs (overnight reactivated with 25 IU per ml IL-2) and allogeneic DOT cells (overnight reactivated with 10 ng ml⁻¹ IL-15) at a 5:1 ratio of effector to target in complete IMDM for 24 h. Then, cells were stained for surface markers followed by caspase 3/7 green (Invitrogen) staining and analyzed in Cytek Aurora (Cytek Biosciences). Data were analyzed with FlowJo software (Tree Star).

In receptor blockade assays, DOT cells were preincubated for 15 min at 4 °C with 20 $\mu\text{g ml}^{-1}$ of either different monoclonal blocking antibodies or equimolar isotype controls, including anti-NKG2D (clone 1D11, BD Biosciences), anti-DNAM1 (clone 11A8, BioLegend), anti-NKp30 (clone P30-15, BioLegend), anti-TCRV δ 1 (clone TS-1), anti-TIGIT (clone A15153G, BioLegend), anti-PD1 (nivolumab, SelleckChem), IgG1 (clone MOPC-21, BioLegend), IgG2a (clone MOPC-173, BioLegend) and IgG4 (clone S228P, MedChemExpress).

DOT cell suppression in vitro assays

To assess the inhibitory functions of PD1 and TIGIT on DOT cells, p96 wells were coated with 10 $\mu\text{g ml}^{-1}$ rCD153/PVR-Fc chimera (BioLegend) and/or rPDL1-Fc chimera (R&D Systems). After washing three times with complete RPMI, 2×10^5 DOT cells were seeded overnight on top in complete RPMI supplemented with 1 ng ml^{-1} IL-15, with or without 10 $\mu\text{g ml}^{-1}$ anti-DNAM1 (clone 11A8, BioLegend) and anti-CD96 (NK92.39, BioLegend) in the presence of 1% brefeldin A (Merck) and 0.1% monensin (Invitrogen).

Orthotopic CRC model

Female nonobese diabetic mice transgenic for human IL-15 were acquired from Taconic (8–14 weeks old; NOD.Cg-Prkdc^{scid} Il2rg^{tm1Sug} Tg(CMV-IL-2/IL-15)1-Ijic/JicTac). Orthotopic GFP + luciferase + SW620 implantation was performed as described previously⁴⁰. Mice were housed in rooms with a light–dark cycle of 14 h and 10 h, respectively, at a temperature of 22–24 °C and relative humidity of 45–65% in specific-pathogen-free animal holding rooms of the GIMM Rodent Facility. Mice were anesthetized with 3% isoflurane in oxygen, administered through the nose cone. The cecum was exposed and 10^5 SW620 cells in 20 μl of PBS were carefully inoculated in the cecal serosa, between the epithelial layers of the cecal wall. After confirmation of successful injection by visualization of a liquid bubble at the site of injection, the cecum was returned to the abdominal cavity. After stitching, 100 μl of a 0.3 mg ml^{-1} buprenorphine solution was subcutaneously administered for analgesia.

Before treatments (day 7 after surgery) and at the indicated time points, tumor growth was measured in an IVIS Lumina fluorescence and bioluminescence imaging system (Caliper, LifeSciences). In brief, mice were anesthetized with an i.p. injection of 200 μl of anesthesia (7.5 mg ml^{-1} ketamine and 0.1 mg ml^{-1} medetomidine in water). Then, abdominal fur was removed and 200 μl of 15 mg ml^{-1} of Xenolight D-luciferin-K⁺ salt bioluminescent substrate (Revvity) was injected i.p. After 7 min, luminescence was measured with 30 and 60 s of exposure. Then, 200 μl of 0.1 mg ml^{-1} Antisedan (Esteve) were administered i.p. for recovery. Luminescence was analyzed by Living Image 3.0 Software. The tumor size was then quantified as the photons released per second. Given that tumors grow intracecally, humane endpoints were defined on the basis of the assessment of body condition and physical appearance and not on tumor size. In this study, humane endpoints were not reached because mice were killed for analysis before symptoms of disease were detected.

In vivo DOT cell treatments

After confirmation of tumor implantation by lumina, mice were randomly assigned to the different treatment groups. In vivo administration of DOT cells was performed i.v. in 100 μl of Optimizer (Gibco). In tumor infiltration kinetics, only one shot of 10^7 DOT cells was administered 3 weeks after tumor implantation and mice were killed at different time points after DOT cell infusion. For therapy experiments, 10^7 DOT cells were infused weekly starting day 7 after tumor implantation and only after confirmation of tumor detection and tumor growth was monitored over time. When indicated, 100 mM sodium butyrate (Sigma) with 1.5% sucrose or 1.5% sucrose only (for control counterparts) was concomitantly administered in the drinking water, replacing the water bottles every 2–3 days. For ICB, mice were i.p. injected

with 50 μg of anti-TIGIT (vibostolimab, Selleckchem) and/or 200 μg of anti-PD1 (nivolumab, Selleckchem) or 50 μg of IgG1 (Selleckchem).

Mouse organ processing for in vivo DOT cell analyses

Mice were killed by CO₂ narcosis at the indicated time points after tumor inoculation and the tumor, blood, spleen, liver, mesenteric lymph nodes, small intestine and remote colon were collected for analysis of DOT cell infiltration and/or phenotype.

Tumors were chopped into small fragments and then incubated with 0.05 mg ml^{-1} collagenase IV (Roche) and 1 mg ml^{-1} DNase I (Roche) for 30 min at 37 °C with 900 rpm agitation in 5 ml of complete IMDM (Gibco) containing 20% FBS, 1% penicillin–streptomycin, 1% amphotericin B (Gibco) and 0.1% 50 mg ml^{-1} Gentamicin (Gibco). Then, single-cell tumor suspensions were passed through a 70- μm filter with the help of a syringe piston, washed with complete IMDM (Gibco) and resuspended in the volume adequate for flow cytometry.

Healthy colon and small intestine tissues were flushed with PBS to remove contents and then opened longitudinally. After being cut into 1-cm pieces, the tissues were incubated at 37 °C for 30 min in PBS containing 20 mM HEPES (Gibco), 100 U per ml penicillin (Gibco), 100 $\mu\text{g ml}^{-1}$ streptomycin (Gibco), 1 mM pyruvate (Gibco), 10% FCS, 100 $\mu\text{g ml}^{-1}$ polymyxin B (Merck) and 10 mM EDTA (Invitrogen) while shaking (15 min at 220 rpm and then reduced to 110 rpm) to release intraepithelial leukocytes (IELs). The IEL suspension was then purified using a 37.5% Percoll gradient (Cytiva) and centrifuged at 700g for 10 min without braking to remove fat tissue. Finally, cells were washed with PBS before proceeding with flow cytometry staining.

Single-cell suspensions of the spleen, liver and blood were incubated with red blood cell lysis buffer (BioLegend) before flow cytometry staining.

Flow cytometry

Single-cell suspensions were incubated in PBS with fluorescently labeled monoclonal antibodies against the different surface markers for 20 min at 4 °C in the dark. For intracellular markers (cytolytic granules and cytokines), cells were fixed and permeabilized for intracellular staining with Foxp3 staining buffer set (Invitrogen) following the manufacturer's instructions. When indicated, cells were stimulated with 0.2 $\mu\text{g ml}^{-1}$ PMA (Merck) + 1 $\mu\text{g ml}^{-1}$ ionomycin (Merck) in the presence of 10 $\mu\text{g ml}^{-1}$ brefeldin A (Merck) + 0.1% monensin (Invitrogen) for 3 h at 37 °C before surface staining for the evaluation of functional intracellular markers.

Flow cytometry acquisition was performed on a BD LSRFortessa X-20 Cell Analyzer (BD Biosciences), BD FACSymphony A5 SE (BD Biosciences) or Cytek Aurora (Cytek) and data were analyzed with FlowJo 10 software (TreeStar). BD FACSDIVA software version 9.0 was used for collection of flow cytometry data. The FlowJo plugin X-shift (version 1.4.1) was used to classify endogenous V δ 1 T cells in different clusters.

For imaging flow cytometry, DOT cells were labeled with CellTrace CFSE (Invitrogen) and tumor cells were labeled with CellTrace Yellow (CTY, Invitrogen) for 10 min at room temperature before a 1-h co-incubation. Cells were then fixed with 1.5% paraformaldehyde and stained with phalloidin AF660 (Invitrogen) during the permeabilization step using PBS containing 0.1% Triton X-100 and 2% FBS. Before acquisition on the Amnis ImageStreamX (Luminex), DAPI was added. Data were analyzed using IDEAS software.

All antibodies and dyes used for flow cytometry are listed in Supplementary Table 2.

Generation of *KLRK1*^{-/-} DOT cells

Two single guide RNAs targeting the *KLRK1* gene (KLRK1 number 1: 5'-ATATCCAGTTTTAGGACAT-3' and KLRK1 number 2: 5'-GCTGTATACTTTCAGAAGGC-3') were designed using the CRISPOR algorithm⁴¹ (<https://crispor.gi.ucsc.edu/>). Corresponding Alt-R CRISPR RNAs (crRNAs) were obtained from Integrated DNA Technologies

(IDT) along with a nontargeting control crRNA and resuspended to 200 μM in TE buffer. crRNAs were then equally mixed with 200 μM Alt-R *trans*-activating crRNA (IDT), annealed by heating for 5 min at 95 °C and cooled to room temperature. These dual gRNAs were individually mixed with 10 μg of Alt-R S.p-Cas9HIFIv3 (IDT) with a 1.6 ratio of gRNA to Cas9. CRISPR–Cas9 knockout was performed cotransfecting with both Cas9 and gRNA ribonucleoproteins as described by Oh et al.⁴² in 10 million cells. *KLRK1* knockout efficiency was evaluated 96 h after transfection according to a lack of expression of NKG2D by flow cytometry.

Upregulation of ligands on tumor cells

For NKG2D ligand upregulation, tumor cells were pretreated for 24 h with 1 mM sodium butyrate (Sigma-Aldrich), 1 mM valproic acid (Merck, PHR1061-1G), 5 μM retinoic acid (Merck, R2625-1G) or 5 nM bortezomib (Merck Millipore, 504314) in complete RPMI.

For evaluation of IFN γ on PD1 and NKR ligand expression, SW620 cells were cultured for 24 h in complete RPMI in the presence of 10 ng ml⁻¹ human rIFN γ (Preprotech) or DOT cells in a 1:1 ratio of DOT to tumor with or without 10 μg ml⁻¹ anti-human IFN γ (clone NIB42, Invitrogen).

SCFA measurement

Cecal contents were collected after 3 weeks of butyrate supplementation in the drinking water. Sample analysis was performed by MS-Omics as follows. Samples were acidified with hydrochloric acid and deuterium-labeled internal standards were added. All samples were analyzed in a randomized order. A high-polarity column (Zebron ZB-FFAP, GC Cap; 30 m \times 0.25 mm \times 0.25 μm) was used for analysis on a gas chromatograph (7890B, Agilent) coupled with a quadrupole detector (5977B, Agilent). The system was controlled by ChemStation (Agilent). Raw data were converted to netCDF format using ChemStation and then imported and processed in Matlab R2021b (MathWorks) using the PARADISE software, as described by Johnsen et al.⁴³.

TCGA gene expression

Data were downloaded using TCGA links for the projects TCGA-COAD (colon adenocarcinoma) and TCGA-LAML (AML). The gene expression was compared within and across datasets after normalization using the fragments per kilobase of transcript per million mapped reads (FPKM).

Statistics and reproducibility

For statistical analysis, the normality of the distributions was assessed using the Shapiro–Wilk test. For normally distributed data, an unpaired Student's *t*-test (or paired *t*-test for matched samples) was used for two-group comparisons or a one-way analysis of variance (ANOVA) with Tukey's multiple-comparisons test was used for comparisons involving more than two groups. For non normal distributions, the Mann–Whitney *U*-test was used for two-group comparisons and the Kruskal–Wallis test with Dunn's multiple-comparisons test was used for multiple groups. In kinetic experiments or when two pairs of groups were analyzed, a two-way ANOVA with Šidák's multiple-comparisons post hoc test was applied. Spearman's correlation coefficient was used to assess the relationship between continuous variables. Data analysis was performed using GraphPad Prism 8.0 (GraphPad Software). *P* values less than 0.05 were considered significant and are presented in the figures.

Sample size was determined throughout the paper on the basis of our experimental observation and experience to guarantee reliable and reproducible results. In the case of human samples, sizes of experiments and analyses were determined by the availability of recruited participant samples at the time of analysis. Sample size is indicated in the figure legends accordingly. No data points meeting technical quality standards were excluded from the analyses. Data collection and analysis were not performed blind to the conditions of the experiments.

Reporting summary

Further information on research design is available in the Nature Portfolio Reporting Summary linked to this article.

Data availability

All TCGA data used in this study were obtained from the publicly available official websites of the project (<http://cancergenome.nih.gov> and <https://portal.gdc.cancer.gov/>). Additional data supporting the findings of this study are available from the corresponding authors on reasonable request. Source data are provided with this paper.

Code availability

No custom code was generated for this study.

References

- Lin, K. X. et al. PD-1 and PD-L1 inhibitors in cold colorectal cancer: challenges and strategies. *Cancer Immunol. Immunother.* **72**, 3875–3893 (2023).
- Nishino, M., Ramaiya, N. H., Hatabu, H. & Hodi, F. S. Monitoring immune-checkpoint blockade: response evaluation and biomarker development. *Nat. Rev. Clin. Oncol.* **14**, 655–668 (2017).
- Ijsselstein, M. E. et al. Revisiting immune escape in colorectal cancer in the era of immunotherapy. *Br. J. Cancer* **120**, 815–818 (2019).
- de Vries, N. L. et al. $\gamma\delta$ T cells are effectors of immunotherapy in cancers with HLA class I defects. *Nature* **613**, 743–750 (2023).
- Mikulak, J. et al. NKp46-expressing human gut-resident intraepithelial $\text{V}\delta 1$ T cell subpopulation exhibits high antitumor activity against colorectal cancer. *JCI Insight* **4**, e125884 (2019).
- Wu, Y. et al. A local human $\text{V}\delta 1$ T cell population is associated with survival in nonsmall-cell lung cancer. *Nat. Cancer* **3**, 696–709 (2022).
- Wu, Y. et al. An innate-like $\text{V}\delta 1^+$ $\gamma\delta$ T cell compartment in the human breast is associated with remission in triple-negative breast cancer. *Sci. Transl. Med.* **11**, eaax9364 (2019).
- Davies, D. et al. PD-1 defines a distinct, functional, tissue-adapted state in $\text{V}\delta 1^+$ T cells with implications for cancer immunotherapy. *Nat. Cancer* **5**, 420–432 (2024).
- Meraviglia, S. et al. Distinctive features of tumor-infiltrating $\gamma\delta$ T lymphocytes in human colorectal cancer. *Oncoimmunology* **6**, e1347742 (2017).
- Yu, L. et al. Tumor-infiltrating $\gamma\delta$ T-cells reveal exhausted subsets with remarkable heterogeneity in colorectal cancer. *Int. J. Cancer* **153**, 1684–1697 (2023).
- Harmon, C. et al. $\gamma\delta$ T cell dichotomy with opposing cytotoxic and wound healing functions in human solid tumors. *Nat. Cancer* **4**, 1122–1137 (2023).
- Mensurado, S., Blanco-Domínguez, R. & Silva-Santos, B. The emerging roles of $\gamma\delta$ T cells in cancer immunotherapy. *Nat. Rev. Clin. Oncol.* **20**, 178–191 (2023).
- Silva-Santos, B. & Mensurado, S. $\gamma\delta$ T cells maintain sensitivity to immunotherapy in MHC-I-deficient tumors. *Nat. Immunol.* **24**, 387–388 (2023).
- Almeida, A. R. et al. Delta One T cells for immunotherapy of chronic lymphocytic leukemia: clinical-grade expansion/differentiation and preclinical proof of concept. *Clin. Cancer Res.* **22**, 5795–5804 (2016).
- Correia, D. V. et al. Differentiation of human peripheral blood $\text{V}\delta 1^+$ T cells expressing the natural cytotoxicity receptor NKp30 for recognition of lymphoid leukemia cells. *Blood* **118**, 992–1001 (2011).
- Di Lorenzo, B. et al. Broad cytotoxic targeting of acute myeloid leukemia by polyclonal Delta One T cells. *Cancer Immunol. Res.* **7**, 552–558 (2019).
- Mensurado, S. et al. CD155/PVR determines acute myeloid leukemia targeting by Delta One T cells. *Blood* **143**, 1488–1495 (2024).

18. Sánchez Martínez, D. et al. Generation and proof-of-concept for allogeneic CD123 CAR-Delta One T (DOT) cells in acute myeloid leukemia. *J. Immunother. Cancer* **10**, e005400 (2022).
19. van der Graaff, D. et al. Advancements in research and treatment applications of patient-derived tumor organoids in colorectal cancer. *Cancers (Basel)* **16**, 2671 (2024).
20. Zhang, K. et al. Bright future or blind alley? CAR-T cell therapy for solid tumors. *Front. Immunol.* **14**, 1045024 (2023).
21. Albarrán, V. et al. Adoptive T cell therapy for solid tumors: current landscape and future challenges. *Front. Immunol.* **15**, 1352805 (2024).
22. Fuertes, M. B., Domaica, C. I. & Zwirner, N. W. Leveraging NKG2D ligands in immuno-oncology. *Front. Immunol.* **12**, 713158 (2021).
23. Gomes, S., Rodrigues, A. C., Paziienza, V. & Preto, A. Modulation of the tumor microenvironment by microbiota-derived short-chain fatty acids: impact in colorectal cancer therapy. *Int. J. Mol. Sci.* **24**, 5069 (2023).
24. He, Y. et al. Gut microbial metabolites facilitate anticancer therapy efficacy by modulating cytotoxic CD8⁺ T cell immunity. *Cell Metab.* **33**, 988–1000 (2021).
25. Rancan, C. et al. Exhausted intratumoral Vδ2⁺ γδ T cells in human kidney cancer retain effector function. *Nat. Immunol.* **24**, 612–624 (2023).
26. Jorgovanovic, D., Song, M., Wang, L. & Zhang, Y. Roles of IFN-γ in tumor progression and regression: a review. *Biomark. Res.* **8**, 49 (2020).
27. Banta, K. L. et al. Mechanistic convergence of the TIGIT and PD-1 inhibitory pathways necessitates co-blockade to optimize anti-tumor CD8⁺ T cell responses. *Immunity* **55**, 512–526 (2022).
28. Watanabe, N., Hizuta, A., Tanaka, N. & Orita, K. Localization of T cell receptor (TCR)-γδ⁺ T cells into human colorectal cancer: flow cytometric analysis of TCR-γδ expression in tumour-infiltrating lymphocytes. *Clin. Exp. Immunol.* **102**, 167–173 (1995).
29. Maeurer, M. J. et al. Human intestinal Vδ1⁺ lymphocytes recognize tumor cells of epithelial origin. *J. Exp. Med.* **183**, 1681–1696 (1996).
30. Chalabi, M. et al. Neoadjuvant immunotherapy in locally advanced mismatch repair-deficient colon cancer. *N. Engl. J. Med.* **390**, 1949–1958 (2024).
31. Verschoor, Y. L. et al. Neoadjuvant nivolumab, ipilimumab, and celecoxib in MMR-proficient and MMR-deficient colon cancers: final clinical analysis of the NICHE study. *J. Clin. Oncol.* **40**, 3511–3511 (2022).
32. Stoeva, M. K. et al. Butyrate-producing human gut symbiont, *Clostridium butyricum*, and its role in health and disease. *Gut Microbes* **13**, 1–28 (2021).
33. Singh, V. et al. Butyrate producers, ‘the sentinel of gut’: their intestinal significance with and beyond butyrate, and prospective use as microbial therapeutics. *Front. Microbiol.* **13**, 1103836 (2022).
34. de Vries, N. L. et al. High-dimensional cytometric analysis of colorectal cancer reveals novel mediators of antitumor immunity. *Gut* **69**, 691–703 (2020).
35. Lien, S. C. et al. Tumor reactive γδ T cells contribute to a complete response to PD-1 blockade in a Merkel cell carcinoma patient. *Nat. Commun.* **15**, 1094 (2024).
36. Stary, V. et al. Dysfunctional tumor-infiltrating Vδ1⁺ T lymphocytes in microsatellite-stable colorectal cancer. *Nat. Commun.* **15**, 6949 (2024).
37. Galletti, G. et al. Two subsets of stem-like CD8⁺ memory T cell progenitors with distinct fate commitments in humans. *Nat. Immunol.* **21**, 1552–1562 (2020).
38. Rodriguez-Abreu, D. et al. Primary analysis of a randomized, double-blind, phase II study of the anti-TIGIT antibody tiragolumab (tira) plus atezolizumab (atezo) versus placebo plus atezo as first-line (1L) treatment in patients with PD-L1-selected NSCLC (CITYSCAPE). *J. Clin. Oncol.* **38**, 9503–9503 (2020).
39. Mensurado, S., Blanco-Domínguez, R., Carreira, M., Barros, L. & Silva-Santos, B. Processing human colon cancer specimens for in vitro cytotoxicity assays. *Methods Cell Biol.* **190**, 105–117 (2024).
40. Blanco-Domínguez, R., Mensurado, S., Barros, L., Carreira, M. & Silva-Santos, B. An orthotopic metastatic xenograft model of colorectal cancer. *Methods Cell Biol.* **190**, 119–132 (2024).
41. Haeussler, M. et al. Evaluation of off-target and on-target scoring algorithms and integration into the guide RNA selection tool CRISPOR. *Genome Biol.* **17**, 148 (2016).
42. Oh, S. A., Seki, A. & Rutz, S. Ribonucleoprotein transfection for CRISPR/Cas9-mediated gene knockout in primary T cells. *Curr. Protoc. Immunol.* **124**, e69 (2019).
43. Johnsen, L. G., Skou, P. B., Khakimov, B. & Bro, R. Gas chromatography–mass spectrometry data processing made easy. *J. Chromatogr. A* **1503**, 57–64 (2017).

Acknowledgements

We acknowledge funding from Takeda Development Center Americas (to B.S.-S., R.B.-D., L.B., M.C., S.M. and C.C.), EMBO Postdoctoral Fellowship (233-2023 to R.B.-D.), Fundação para a Ciência e Tecnologia (FCT), Ministério da Ciência, Tecnologia e Ensino Superior (PTDC/MED-ONC/6829/2020 to B.S.-S. and L.B.; 2021.01953.CEECIND to S.M.), Liga Portuguesa Contra o Cancro NRS (‘Dissecting the impact of the TME on DOT cells towards maximizing their therapeutic potential in CRC’ to R. B.-D., L.B., C.C. and S.M.) and Institut National contre le Cancer, Fondation ARC and LNCC (PAIR-2021-199 to J.D.-M.). We were also supported by iMM-CARE, funded by the European Union’s Horizon Europe research and innovation program under grant number 101060102 and cofunded by the Portuguese Government, the FCT, the Francisco Manuel dos Santos Society Group (ARICA, Investimentos, Participações e Gestão and Jerónimo Martins), the Gulbenkian Institute for Molecular Medicine and the Lisbon Academic Medical Center. The funders had no role in study design, data collection and analysis, decision to publish or preparation of the manuscript. We thank N. Barbosa-Morais and the staff of the Flow Cytometry, Bioimaging and Rodent Facilities and the Biobank (especially Â. Afonso) of the Gulbenkian Institute for Molecular Medicine, as well as the staff of the CRISPR edit technology platform (INSERM US 005, CNRS UAR 3427- TBMCore, Université de Bordeaux) and R. van der Breggen from Leids Universitair Medisch Centrum, for their technical support and assistance. We thank the Colorectal Surgery, Anatomical Pathology and Gastroenterology divisions from the Hospital Santa Maria (namely, R. T. Marinho, L. Miranda, J. Malaquias, T. Pereira, S. Fernandes, R. Esteves and R. M. Cruz) and other doctors, nurses and technicians who were essential for the provision of primary CRC samples. We thank the participants with CRC and their families.

Author contributions

R.B.-D., L.B. and M.C. performed most of the experiments and analyzed the data. M.v.d.P., C.C. and S.M. assisted with some experiments. R.B.-D., S.M. and B.S.-S. designed the experiments. C.F., C.C., C.M.F. and N.F.C.C.d.M. provided human specimens. G.M. and J.D.-M. generated *KLRK1*-knockout DOT cells. B.S.-S. conceptualized the study. R.B.-D. and B.S.-S. wrote the paper. S.M., M.C. L.B. and N.F.C.C.d.M. revised the paper and provided critical feedback.

Competing interests

B.S.-S., R.B.-D., L.B., M.C., S.M., and C.C. received funding from a sponsored research agreement with Takeda Development Center Americas. The other authors declare no competing interests.

Additional information

Extended data is available for this paper at <https://doi.org/10.1038/s43018-025-00948-9>.

Supplementary information The online version contains supplementary material available at <https://doi.org/10.1038/s43018-025-00948-9>.

Correspondence and requests for materials should be addressed to Rafael Blanco-Domínguez or Bruno Silva-Santos.

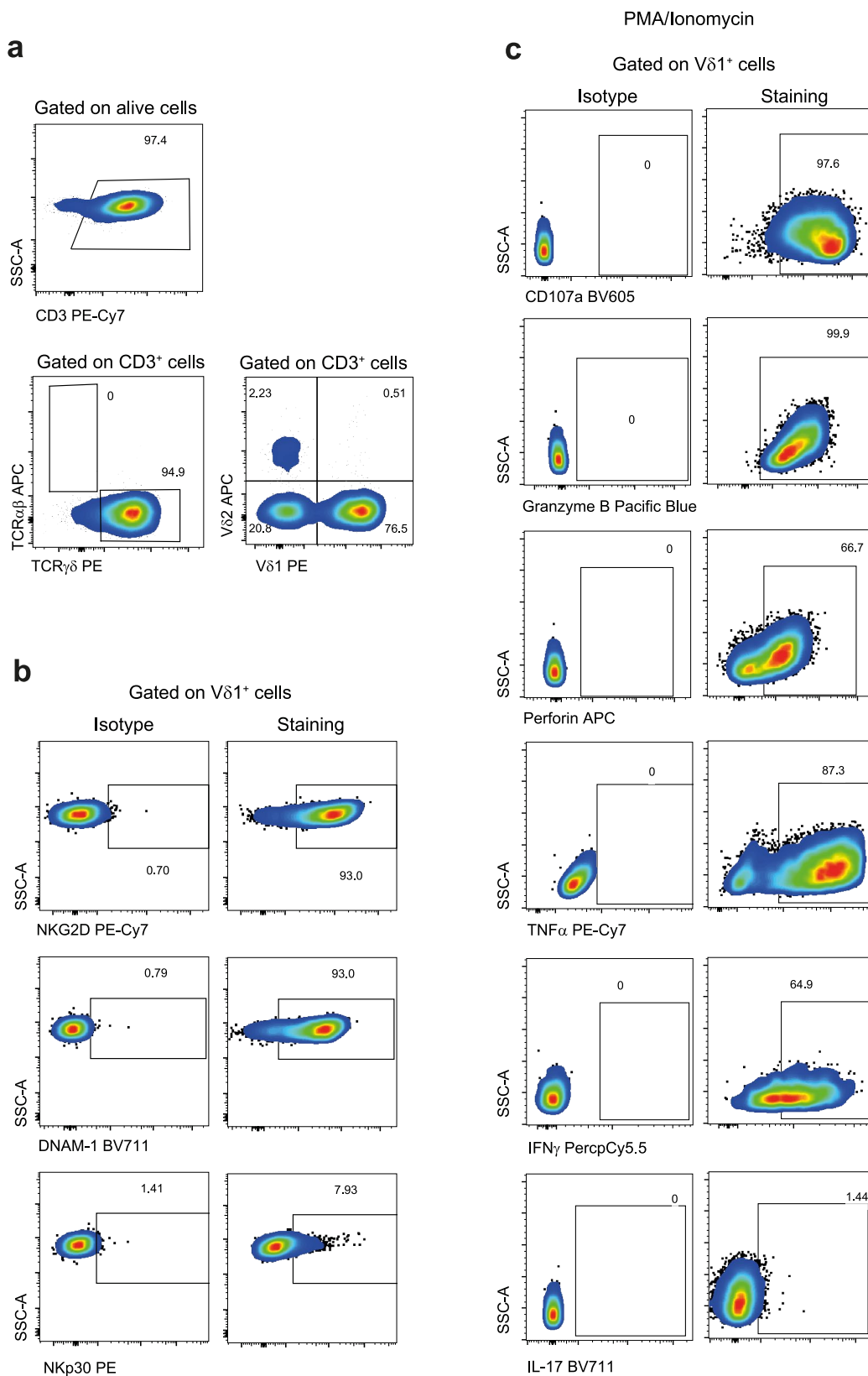
Peer review information *Nature Cancer* thanks Rene Jackstadt, Dieter Kabelitz and the other, anonymous, reviewer(s) for their contribution to the peer review of this work.

Reprints and permissions information is available at www.nature.com/reprints.

Publisher's note Springer Nature remains neutral with regard to jurisdictional claims in published maps and institutional affiliations.

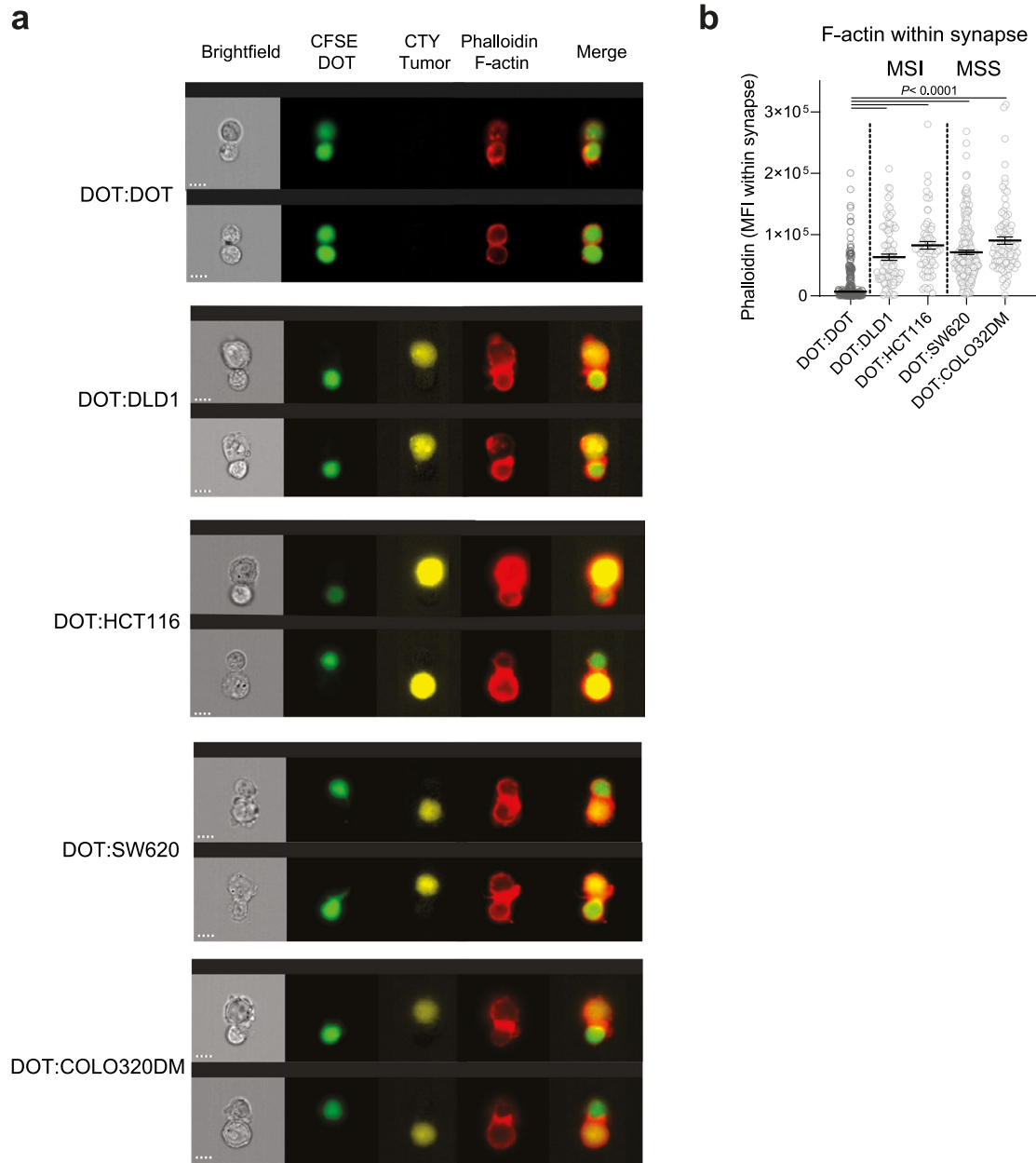
Open Access This article is licensed under a Creative Commons Attribution-NonCommercial-NoDerivatives 4.0 International License, which permits any non-commercial use, sharing, distribution and reproduction in any medium or format, as long as you give appropriate credit to the original author(s) and the source, provide a link to the Creative Commons licence, and indicate if you modified the licensed material. You do not have permission under this licence to share adapted material derived from this article or parts of it. The images or other third party material in this article are included in the article's Creative Commons licence, unless indicated otherwise in a credit line to the material. If material is not included in the article's Creative Commons licence and your intended use is not permitted by statutory regulation or exceeds the permitted use, you will need to obtain permission directly from the copyright holder. To view a copy of this licence, visit <http://creativecommons.org/licenses/by-nc-nd/4.0/>.

© The Author(s) 2025



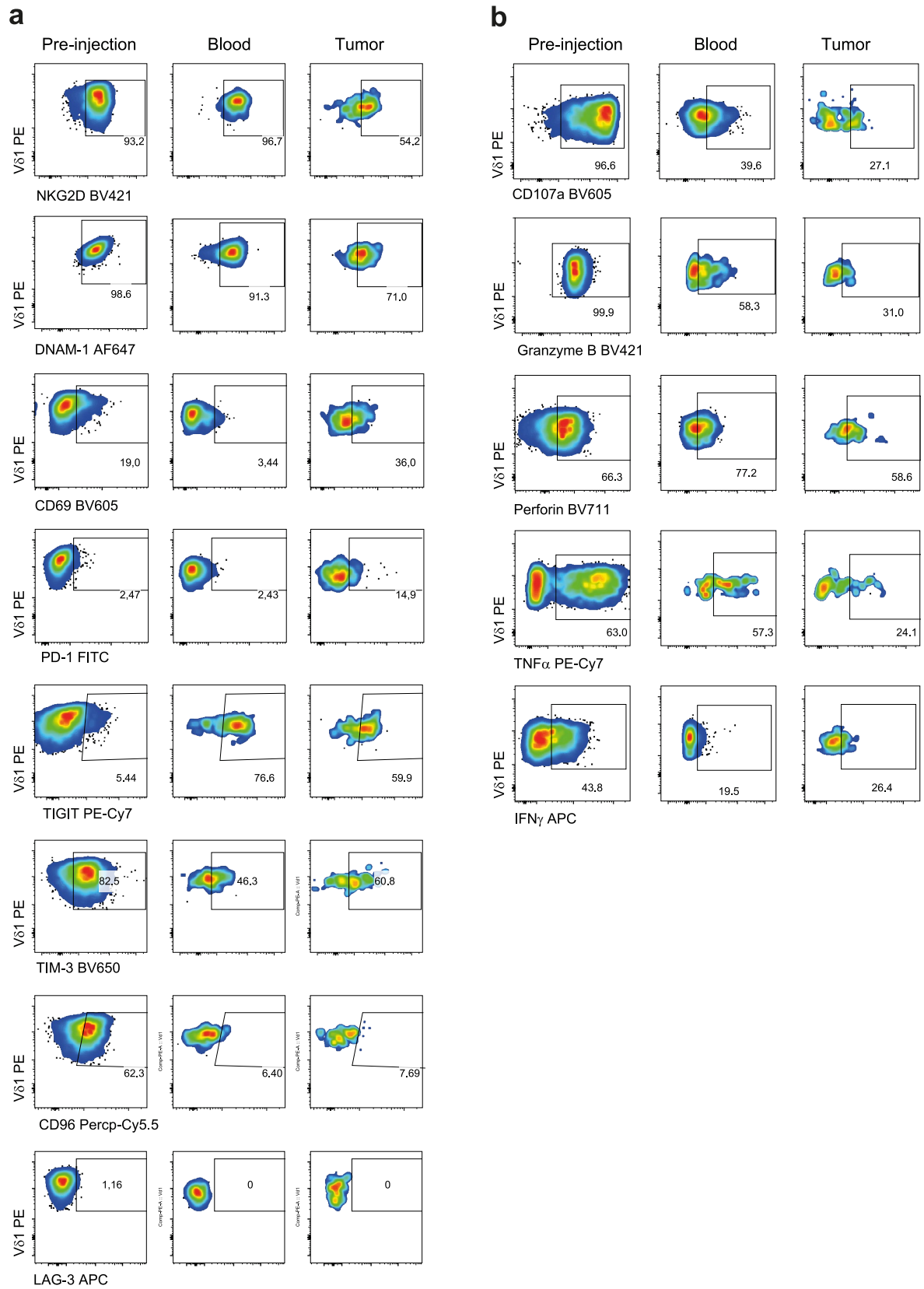
Extended Data Fig. 1 | DOT-cell phenotype. (a) Density plots represent an example of the purity of $\gamma\delta$ T cells and V δ 1⁺ T cells after DOT cell expansion/differentiation from PBMCs from healthy volunteers (b) Representative percentages of NKG2D, DNAM-1 and Nkp30, gated on V δ 1⁺ T cells. (c)

Degranulation (CD107a), Granzyme B and Perforin production and cytokine expression after 3h PMA/Ionomycin stimulation in the presence of protein translocator inhibitors in a representative DOT donor.



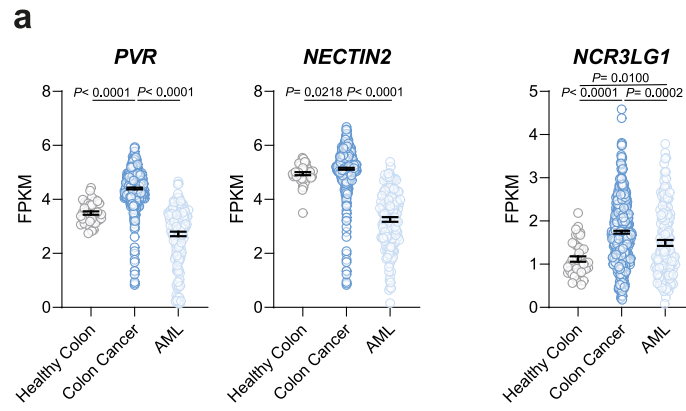
Extended Data Fig. 2 | DOT cells establish immunological synapses with both MSI and MSS CRC cell lines. (a) Representative images of image flow cytometry data of immunological synapses formed between DOT cells and different CRC cell lines. (b) Quantification of filamentous actin (F-actin) signal within the area

of interaction between DOT cells and tumor cells (n= 88 HCT116, n= 64 DLD1, n=183 SW620, n= 89 COLO320 doublets), compared with the signal in DOT:DOT cell doublets (n= 183 doublets). Data represented as means \pm SEM and were analyzed with Kruskal-Wallis with Dunn's multiple comparisons test.

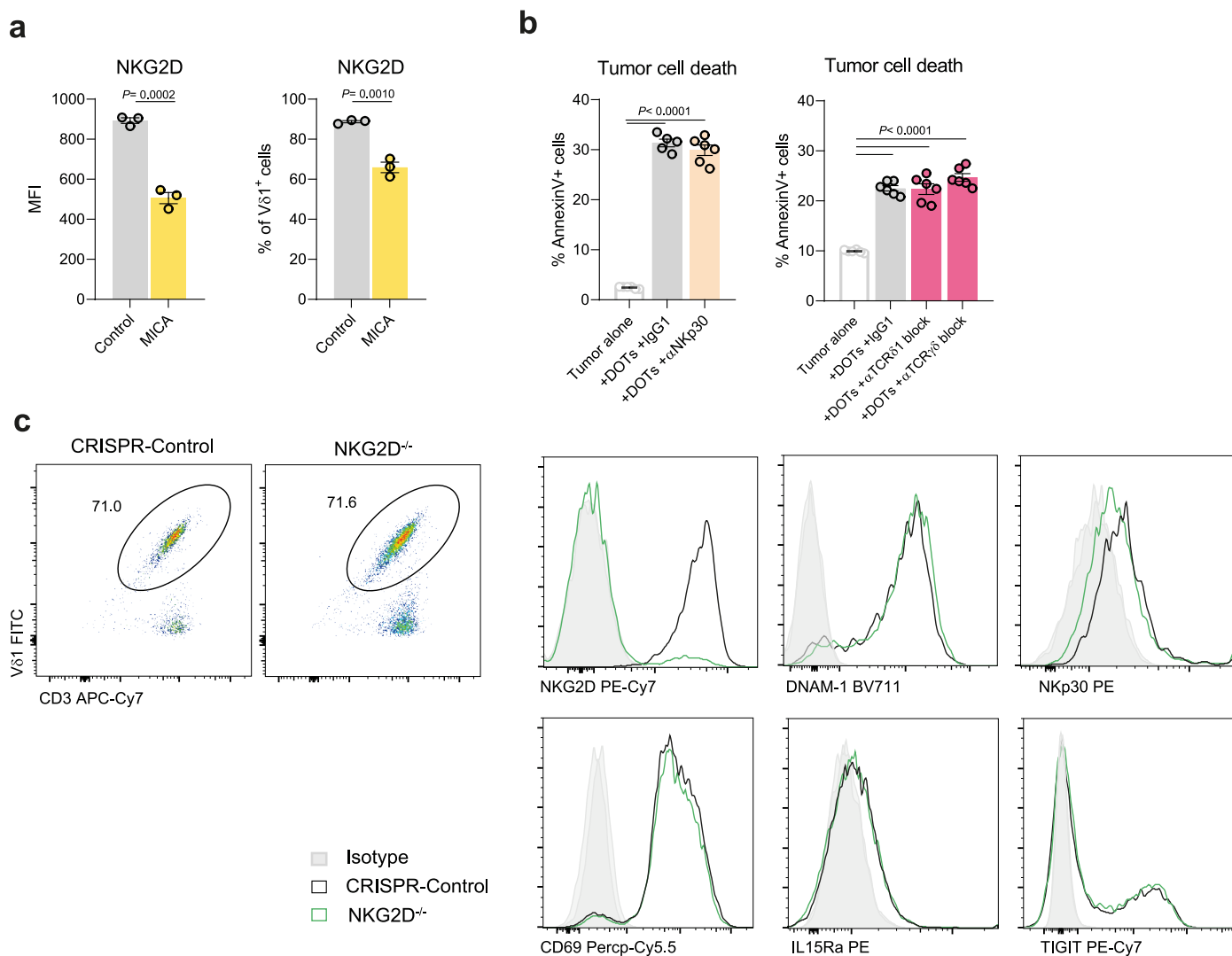


Extended Data Fig. 3 | In vivo expression of inhibitory, activation and cytotoxicity receptors in DOT cells. Flow cytometry density plots show representative percentages of DOT cells before infusion and in the tumor and in the blood 14 days after infusion into intercaecal SW620-bearing mice, after

gating on alive human CD45+CD3+Vδ1+ cells (a) Surface markers were stained in fresh. (b) CD107a and intracellular staining were stained after 3h of PMA/Ionomycin stimulation in the presence of Brefeldin A and Monensin.



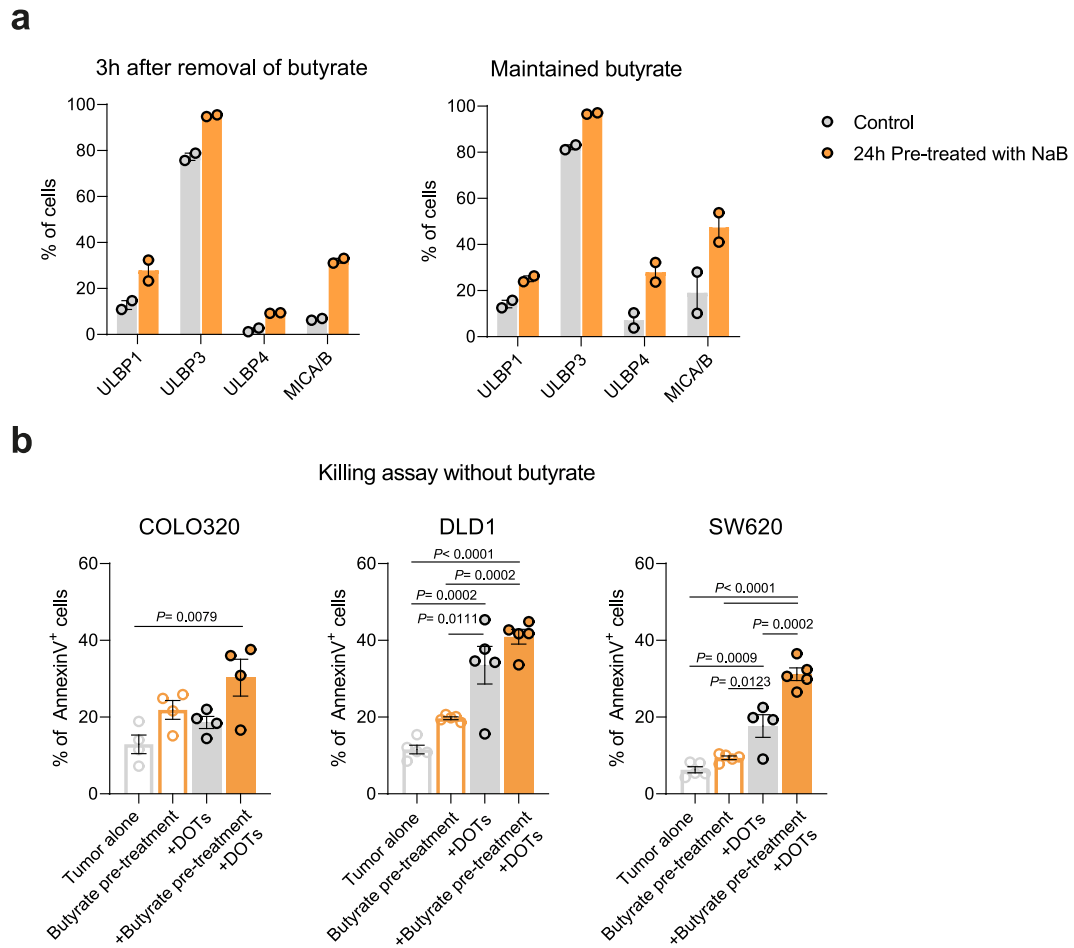
Extended Data Fig. 4 | DNAM-1 and Nkp30 ligand expression in colon cancer. (a) Expression of DNAM-1 and Nkp30 ligands in colon cancers (n= 453 patients) versus healthy colon tissue (n= 41 donors). Data represented as means \pm SEM and were analyzed by two-tailed Mann-Whitney U-test.



Extended Data Fig. 5 | NKG2D is important for CRC targeting by DOT cells.

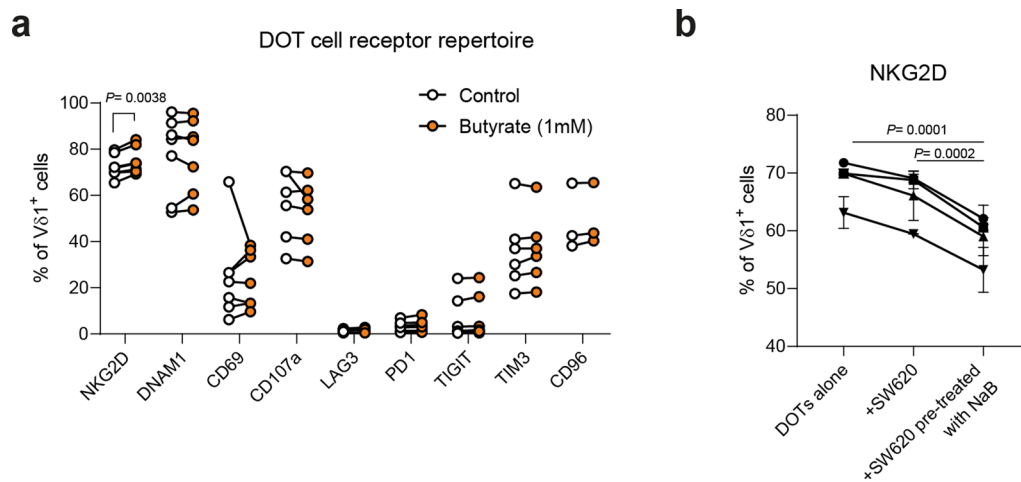
(a) Mean fluorescence intensity (MFI) and percentage of NKG2D⁺ cells in DOT cells after incubation with plate-bound MICA Fc-chimera for 48h (n=3 technical replicates from the same donor). Two-tailed unpaired t-test. One representative out of two independent experiments. (b) 3h-Killing assay of SW620 cells incubated with medium (tumor alone, n=6 DOT donors) or with DOT cells in the presence of either αNkp30 (n=6 technical replicates), αTCRδ1 (clone TS-1) (n=6 DOT donors) or αTCRγδ (clone B.1) (n=6 DOT donors) blocking antibody or their

isotype controls (n=5 DOT donors left, and n=6 DOT donors right), quantified by flow cytometry Annexin V staining. Data points represent individual replicates from two DOT donors. One-way ANOVA with Tukey's post-hoc test. Pool of three independent experiments. Data represented as means ± SEM. (c) Phenotype of NKG2D^{-/-} DOT cells and CRISPR-Cas9 controls. Representative percentage of CD3⁺Vδ1⁺ cells after gating on alive cells is shown. Histograms represent expression of different receptors after gating on Vδ1⁺ cells.



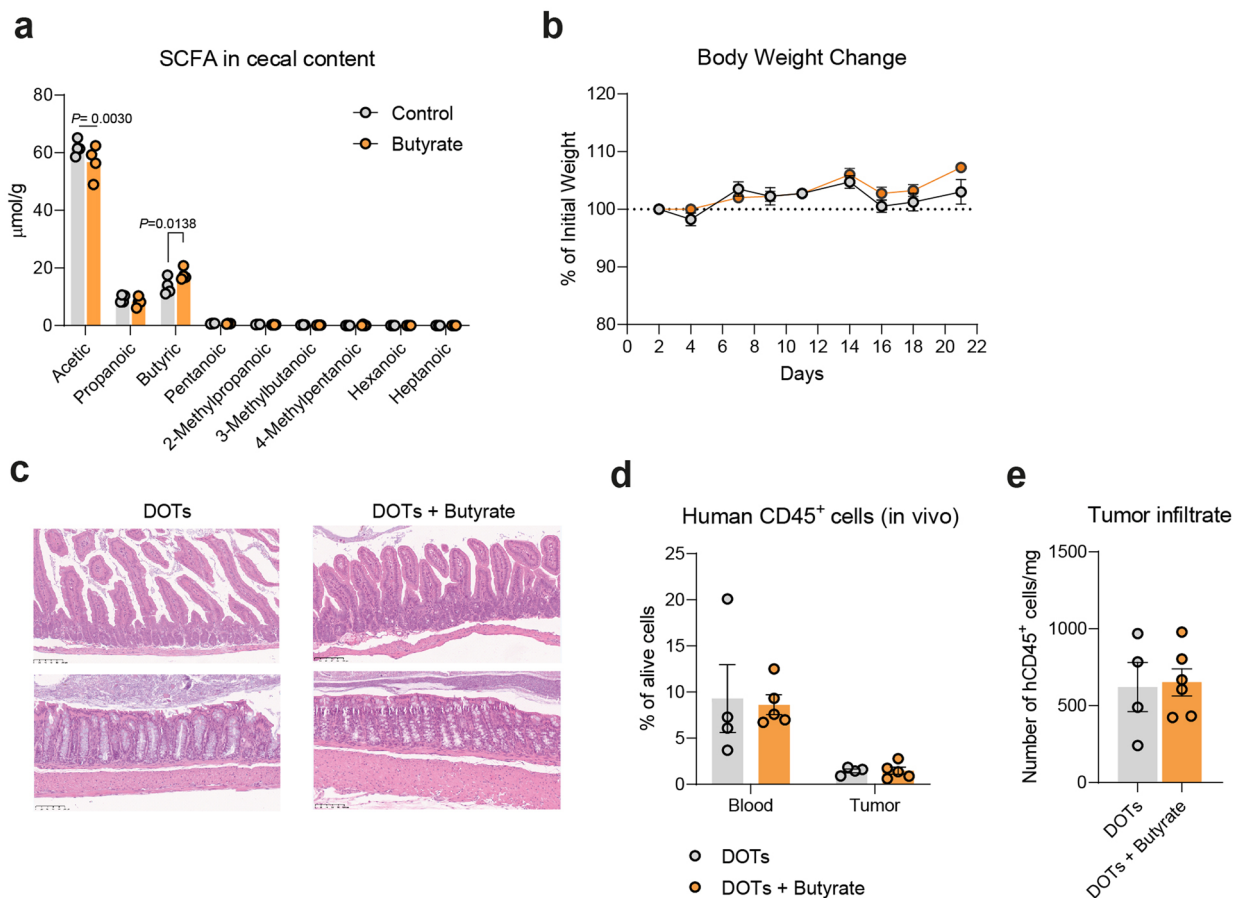
Extended Data Fig. 6 | Butyrate enhances DOT-cell targeting of CRC cells. (a) Expression of NKG2D ligands in SW620 cells, assessed by flow cytometry, with or without exposure to butyrate for 24h and with (right) or without (left) additional 3h-exposure to butyrate (n=2 technical replicates). One representative out of three independent experiments with similar results. **(b)** Different CRC cell

lines were pre-treated with butyrate (for 24h) and then a 3h-killing assay was performed in the absence of butyrate. Each point represents individual DOT donors (n=4 DOT donors for COLO320, n=5 DOT donors for DLD1 and SW620). One-way ANOVA with Tukey's post-hoc test. One representative out of three independent experiments.



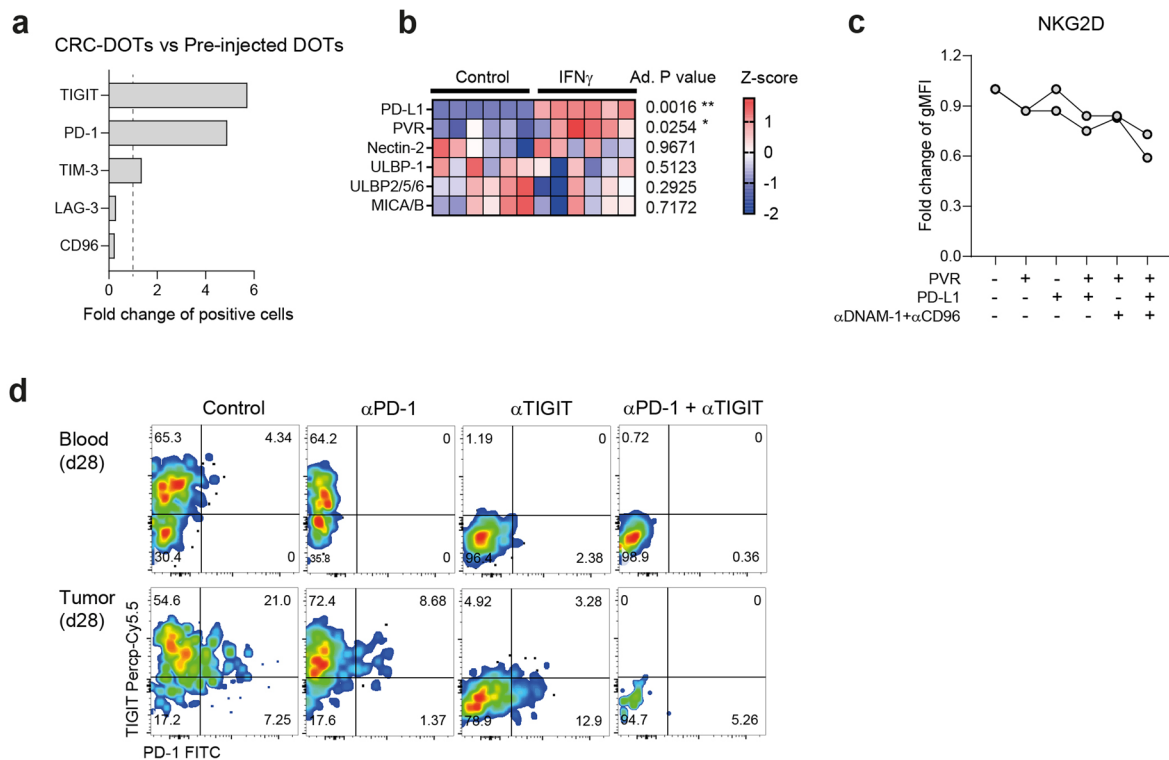
Extended Data Fig. 7 | Butyrate favors NKG2D-NKG2D-L interactions. (a) DOT-cell receptor repertoire in the presence or absence of butyrate for 3h. Individual DOT cell donors are connected with lines (n= 3 DOT donors for CD96; n= 6 DOT donor for PD-1, LAG-3, CD107a, TIGIT and TIM3; n= 7 DOT donors for NKG2D, DNAM-1 and CD69). Analyzed by repeated-measures one-way ANOVA with

Tukey's post-hoc test. Pool of three assays. (b) NKG2D+ DOT cells, assessed by flow cytometry, in contact with SW620 cells that were or were not pre-incubated for 24h with butyrate. Data represented as means \pm SEM of technical replicates, symbols depict different DOT donors (n= 3 DOT donors). One-way ANOVA with Tukey's post-hoc test.



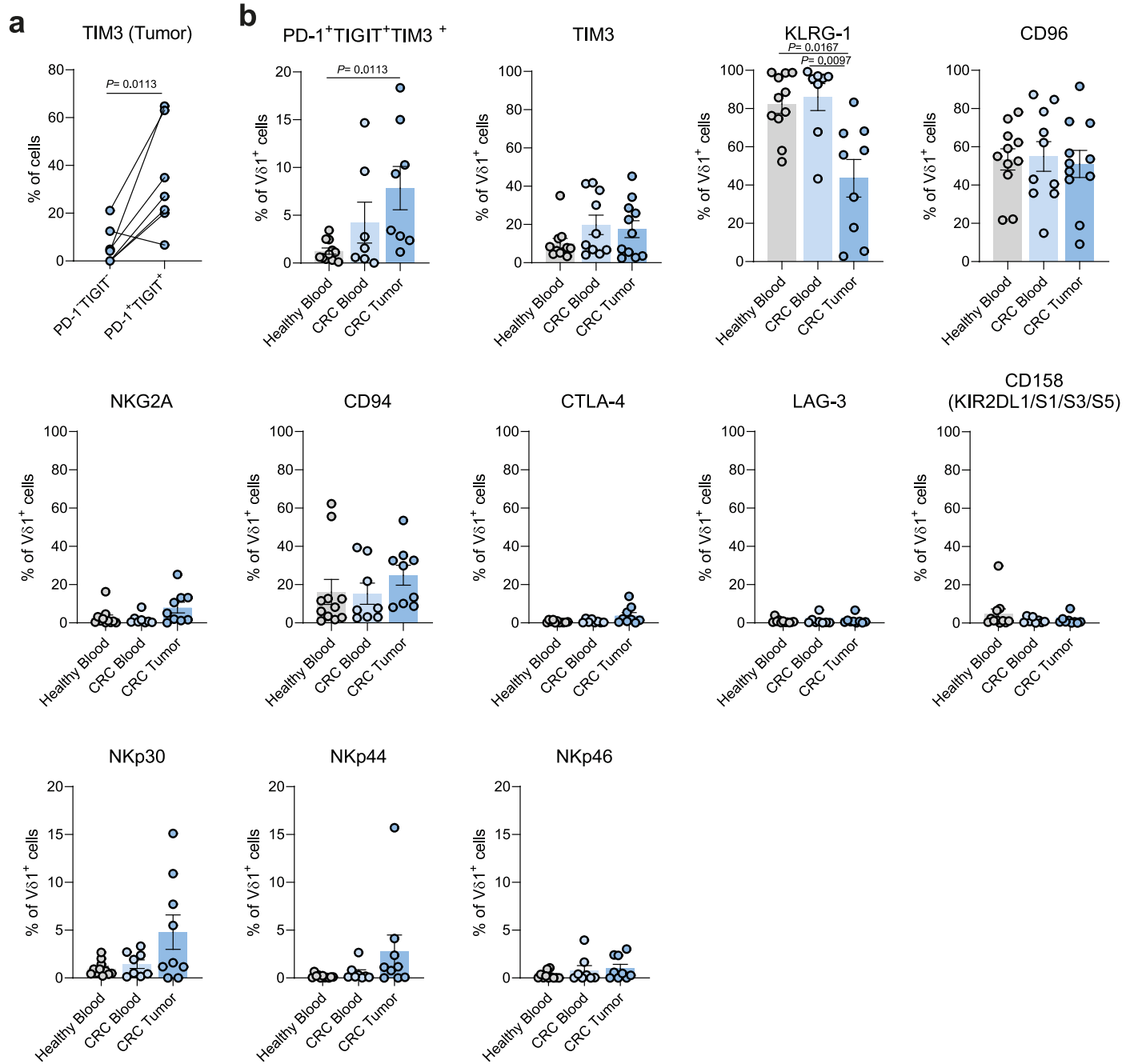
Extended Data Fig. 8 | Butyrate administration is safe and does not impact DOT-cell infiltration in the tumor. (a) Levels of short-chain fatty acids in the cecal content of mice treated with butyrate (100 mM) and sucrose (1.5%) in the drinking water or control mice receiving with only sucrose, three weeks after treatment onset ($n=4$ mice per group). Two-way ANOVA with Sidak's multiple comparisons test. (b) Percentage of body weight change over time (versus the initial weight) of mice treated with butyrate in the drinking water or control mice ($n=4$ mice per group). Data represented as means \pm SEM. (c) Representative

images of the intestinal track of control and butyrate treated mice, 30 days after tumor inoculation and 21 days after treatment onset. (d) Percentage of DOT cells, assessed by human CD45 expression by flow cytometry, in the blood and tumor of butyrate-treated mice ($n=5$ mice) and controls ($n=4$ mice) at day 28 post intercaecal SW620-inoculation. One representative out of two independent experiments. (e) DOT-cell numbers per mg of tumor at day 28 post intercaecal SW620 cell-inoculation ($n=4$ mice treated with DOTs, $n=5$ mice treated with DOTs + Butyrate). Data represented as means \pm SEM.



Extended Data Fig. 9 | IFN γ exposure upregulates PD-L1 and PVR levels on SW620 cells. (a) Differential expression, assessed by flow cytometry, of checkpoint receptors on DOT cells infiltrating the intercaecal SW620 tumors and before infusion, represented as fold change of positive cells in the tumor versus pre-injection. (b) Heatmap shows the surface expression of different ligands with or without exposure to IFN γ for 24h (n= 6 replicated plate wells). The color scale represents the Z-score of the geometric mean of fluorescence intensity. Two-way ANOVA with Sidak's multiple comparisons test. One representative

out of two independent experiments. (c) NKG2D levels after 24h incubation with plate-bound PVR and/or PD-L1 in the presence or not of αDNAM-1/αCD96 blocking antibodies (mean of technical replicates from n=2 independent experiments). Analyzed by one-way ANOVA with Tukey's post-hoc test. Data represented as means ± SEM. (d) Representative flow cytometry density plots of PD-1 and TIGIT expression in blood and tumor-infiltrating DOT cells, at day 28 after tumor injection upon in vivo checkpoint blockade (gated on alive human CD45+CD3+TCRVδ1+ cells).



Extended Data Fig. 10 | Receptor repertoire of endogenous V δ 1⁺ T cells in CRC. (a) Expression of TIM3 in PD1-TIGIT⁻ and PD1⁺TIGIT⁺ V δ 1⁺ T cells in blood and tumors from CRC patients (connected points of n=7 patients). Data were analyzed by two-tailed paired t-test. (b) Quantification of expression of different inhibitory and cytotoxic receptors in blood from healthy controls and blood and

tumors from CRC patients (n= 11 samples), represented as percentage of positive cells among alive V δ 1⁺ cells. Data analyzed by one-way ANOVA with Tukey's post hoc test or Kruskal-Wallis with Dunn multiple comparisons test. Representative of three independent experiments.

Reporting Summary

Nature Portfolio wishes to improve the reproducibility of the work that we publish. This form provides structure for consistency and transparency in reporting. For further information on Nature Portfolio policies, see our [Editorial Policies](#) and the [Editorial Policy Checklist](#).

Statistics

For all statistical analyses, confirm that the following items are present in the figure legend, table legend, main text, or Methods section.

n/a | Confirmed

- The exact sample size (n) for each experimental group/condition, given as a discrete number and unit of measurement
- A statement on whether measurements were taken from distinct samples or whether the same sample was measured repeatedly
- The statistical test(s) used AND whether they are one- or two-sided
Only common tests should be described solely by name; describe more complex techniques in the Methods section.
- A description of all covariates tested
- A description of any assumptions or corrections, such as tests of normality and adjustment for multiple comparisons
- A full description of the statistical parameters including central tendency (e.g. means) or other basic estimates (e.g. regression coefficient) AND variation (e.g. standard deviation) or associated estimates of uncertainty (e.g. confidence intervals)
- For null hypothesis testing, the test statistic (e.g. F , t , r) with confidence intervals, effect sizes, degrees of freedom and P value noted
Give P values as exact values whenever suitable.
- For Bayesian analysis, information on the choice of priors and Markov chain Monte Carlo settings
- For hierarchical and complex designs, identification of the appropriate level for tests and full reporting of outcomes
- Estimates of effect sizes (e.g. Cohen's d , Pearson's r), indicating how they were calculated

Our web collection on [statistics for biologists](#) contains articles on many of the points above.

Software and code

Policy information about [availability of computer code](#)

Data collection

No custom code was used to collect the data
BD FACSDIVA software version 9.0 was used for collection of flow cytometry data.

Data analysis

All analyses are described in the relevant section of Methods.
For flow cytometry data, data were analyzed with FlowJo software v10.10.0. The FlowJo plugin X-shift (version 1.4.1) was used to classify endogenous V δ 1 T cells in different clusters.
For statistical analyses and graphs, GraphPad Prism v8.4.0

For manuscripts utilizing custom algorithms or software that are central to the research but not yet described in published literature, software must be made available to editors and reviewers. We strongly encourage code deposition in a community repository (e.g. GitHub). See the Nature Portfolio [guidelines for submitting code & software](#) for further information.

Data

Policy information about [availability of data](#)

All manuscripts must include a [data availability statement](#). This statement should provide the following information, where applicable:

- Accession codes, unique identifiers, or web links for publicly available datasets
- A description of any restrictions on data availability
- For clinical datasets or third party data, please ensure that the statement adheres to our [policy](#)

This study includes no data deposited in external repositories. Source data are provided with this paper. All cancer patient and TCGA data were obtained from the publicly available official websites of the project (<http://cancergenome.nih.gov> and <https://portal.gdc.cancer.gov/>). Additional data supporting the findings of this study are available from the corresponding authors on reasonable request.

Research involving human participants, their data, or biological material

Policy information about studies with [human participants or human data](#). See also policy information about [sex, gender \(identity/presentation\), and sexual orientation](#) and [race, ethnicity and racism](#).

Reporting on sex and gender	Sex and gender are not considered in the study design of human samples, which includes biological male and female sexes.
Reporting on race, ethnicity, or other socially relevant groupings	We did not consider race, ethnicity or other socially relevant grouping in our analyses.
Population characteristics	Both colon and rectal cancer patients ranged between 52 and 85 years old and were not subjected to any treatment.
Recruitment	Colon and rectal tumor specimens from patients were prospectively collected by colonoscopy (at the time of tumor resection) and prior to treatment between January 2023 and March 2024 from the Hospital Santa Maria (Lisbon, Portugal). In addition, a blood sample was collected from the same patients and PBMCs were cryopreserved at the biobank of the Instituto de Medicina Molecular João Lobo Antunes. In parallel, blood samples from 11 randomized age-matched healthy donors from the biobank were analyzed. Seven patient-derived organoids and tumor-infiltrating leukocytes expanded from CRC patients (four MMRp/MSS and three MMRd/MSI) at the Leiden University Medical Center as described below were included in this work. Patient samples were anonymized and handled according to the medical ethical guidelines described in the Code of Conduct for Proper Secondary Use of Human Tissue of the Dutch Federation of Biomedical Scientific Societies.
Ethics oversight	This investigator-initiated study was conducted in accordance with the principles of the Declaration of Helsinki and the International Conference on Harmonization Good Clinical Practice guidelines and was approved by the ethics committee of Centro Académico de Medicina de Lisboa (no. 329/20 and 329/20/21A). All patients included in the study provided written informed consent before sample collection. Participants were not compensated for study participation.

Note that full information on the approval of the study protocol must also be provided in the manuscript.

Field-specific reporting

Please select the one below that is the best fit for your research. If you are not sure, read the appropriate sections before making your selection.

Life sciences Behavioural & social sciences Ecological, evolutionary & environmental sciences

For a reference copy of the document with all sections, see nature.com/documents/nr-reporting-summary-flat.pdf

Life sciences study design

All studies must disclose on these points even when the disclosure is negative.

Sample size	Sample size was determined throughout the manuscript based on our experimental observation and experience to guarantee reliable and reproducible results. In the case of human samples, size of experiments and analyses was determined by the availability of recruited patient samples at the time of analysis. Sample size is indicated in the figure legends accordingly.
Data exclusions	No data were excluded from analyses
Replication	At least 3 biological and/or technical replicates were used for all our experiment as it is described in the figure legends. For in vivo experiments and patient samples, biological replicates are always represented. For in vitro killing assays, biologically replicated DOT donors are used. For induction of ligand expression on tumor cell lines, technical replicates were used.
Randomization	Mice were randomly assigned to the different groups.
Blinding	Data collection and analysis were not performed blind to the conditions of the experiments

Reporting for specific materials, systems and methods

We require information from authors about some types of materials, experimental systems and methods used in many studies. Here, indicate whether each material, system or method listed is relevant to your study. If you are not sure if a list item applies to your research, read the appropriate section before selecting a response.

Materials & experimental systems

n/a	Involved in the study
<input type="checkbox"/>	<input checked="" type="checkbox"/> Antibodies
<input type="checkbox"/>	<input checked="" type="checkbox"/> Eukaryotic cell lines
<input checked="" type="checkbox"/>	<input type="checkbox"/> Palaeontology and archaeology
<input type="checkbox"/>	<input checked="" type="checkbox"/> Animals and other organisms
<input checked="" type="checkbox"/>	<input type="checkbox"/> Clinical data
<input checked="" type="checkbox"/>	<input type="checkbox"/> Dual use research of concern
<input checked="" type="checkbox"/>	<input type="checkbox"/> Plants

Methods

n/a	Involved in the study
<input checked="" type="checkbox"/>	<input type="checkbox"/> ChIP-seq
<input type="checkbox"/>	<input checked="" type="checkbox"/> Flow cytometry
<input checked="" type="checkbox"/>	<input type="checkbox"/> MRI-based neuroimaging

Antibodies

Antibodies used

Marker /Fluorochrome / Clone / Company / Reference /Dilution Factor

B7-H6 PE 875001 R&D Systems FAB144P-100 15
 CD107a BV605 H4A3 Biolegend 328634 200
 CD158 (KIR2D) BUV395 HP-MA4 BD 567326 200
 CD3 BUV805 SK7 BD 612894 200
 CD3 BV510 OKT3 Biolegend 317332 200
 CD45 PE-CF594 HI30 BD 562279 400
 CD45 AF700 HI30 Biolegend 304023/4 200
 CD45 PEDzle 2D1 Biolegend 368529/30 200
 CD69 RB744 FN50 BD 570501 100
 CD69 BV605 FN50 Biolegend 310937/8 100
 CD69 PERCPy5.5 FN50 BioLegend 310925 100
 CD94 PE HP-3D9 BD 555889 100
 CD96 APC NK92.39 BioLegend 338409 100
 CD96 BV421 6F9 BD 742794 100
 CD96 PercpCy5.5 NK92.39 BioLegend 338411 100
 CTLA4//CD152 RY586 BNI3 BD 568442 100
 DNAM1 FITC 11A8 BioLegend 338304 100
 DNAM-1 BV711 11A8 BioLegend 338333 100
 Gzmb Pacific blue GB11 BioLegend 515408 200
 IFNg APC 4S.B3 Invitrogen 51-7319-42 100
 IFNg APC 4S.B3 BioLegend 502512 100
 IFNg PercpCy5.5 4S.B3 BioLegend 502526 100
 KLRG1 RB780 Z7-205.rMAb BD 569137 100
 LAG-3 APC-R700 T47-530 BD 565775 100
 LAG-3 APC 3DS223H Invitrogen 17-2239-42 100
 MICA/B BV711 6D4 BD 742326 4
 Nectin-2 APC TX31 BioLegend 337412 20
 Nectin-2 Percp-Cy5.5 TX31 BioLegend 337415 20
 NKG2a BB700 131411 BD 747926 100
 NKG2D BV421 1D11 BioLegend 320822 100
 NKG2D BV785 1D11 BioLegend 320830 100
 NKG2D PECy7 1D11 BioLegend 320812 100
 NKp30 BUV737 P30-15 BD 749128 100
 NKp30 APC P30-15 BioLegend 325210 100
 NKp44 BUV615 P44-8 BD 752353 100
 NKp46 AF647 9.00E+02 Biolegend 331910 100
 PD1 APCCy7 EH12.2H7 BioLegend 329921 100
 PD1 BV480 EH12.1 BD 566112 50
 PD1 FITC MIH4 Invitrogen 11-9969-42 50
 PD-L1 APC 29E.2A3 BD 568315 100
 Perforin BV711 dG9 Sony 2140645 100
 PVR PECy7 SKII.4 BioLegend 337614 40
 TIGIT PECy7 A15153G BioLegend 372713 200
 TIGIT PercpCy5.5 A15153G BioLegend 372717 100
 TIM3 BV650 7D3 BD 565564 100
 TNF BUV395 Mab11 BD 563996 200
 TNF PECy7 Mab11 Biolegend 502930 200
 ULBP-1 PERCP 170818 R&D Systems FAB1380C 5
 ULBP-2/5/6 BV605 165903 BD 748131 7

ULBP3 AF405 166510 R&D Systems FAB1517V 5
 ULBP-4 AF750 709116 R&D Systems FAB6285S 15
 Vd1 PE REA173 Miltenyi 130-120-440 200
 Vd1 FITC REA173 Miltenyi 130-118-362 100
 Vd1 APC REA173 Miltenyi 130-119-145 200
 Vd2 APC-Vio770 REA771 Miltenyi 130-111-130 200
 IgG1 BV785 MOPC-21 BioLegend 400169 equimolar
 IgG1 BV711 MOPC-21 BioLegend 400167 equimolar
 IgG1 BV421 X40 BD 400157 equimolar
 IgG1 BV650 X40 BD 563231 equimolar
 IgG1 FITC MOPC-21 BioLegend 400108 equimolar
 IgG1 RB744 X40 BD 570519 equimolar
 IgG1 BV605 MOPC-21 BioLegend 400161 equimolar
 IgG1 APC-R700 X40 BD 564974 equimolar
 IgG1 BUV737 X40 BD 612758 equimolar
 IgG1 PE MOPC-21 BioLegend 400112 equimolar
 IgG1 BUV615 X40 BD 612986 equimolar
 IgG1 RB780 X40 BD 568532 equimolar
 IgG1 PercpCy5.5 MOPC-21 BioLegend 400149 equimolar
 IgG1 PECy7 MOPC-21 BioLegend 400125 equimolar
 IgG2a PECy7 MOPC-173 BioLegend 400232 equimolar
 IgG2a BB700 G155-178 BD 566419 equimolar
 IgG2a RY586 G155-178 BD 568131 equimolar
 IgG2a AF405 20102 R&D Systems IC003V equimolar
 IgG2a BV605 G155-178 BD 562778 equimolar
 IgG2a BV711 G155-178 BD 563345 equimolar
 IgG2b BUV395 27-35 BD 563558 equimolar
 IgG2b APC MPC-11 BioLegend 400322 equimolar
 IgG2b AF750 133303 R&D Systems IC0041S equimolar

Mouse CD11b APCCy7 M1/70 BioLegend 101226 200
 Mouse CD11b BV711 M1/70 BioLegend 101241 200
 mouseCD45 PEDdzzle 30-F11 BioLegend 103146 200
 mouseCD45 BV510 30-F11 BioLegend 103137 200

Zombie Violet BioLegend 423114 500
 Zombie Acqua BioLegend 423102 500
 Live/Dead NIR Invitrogen L34976 5000
 Annexin V AF647 BioLegend 640912 100
 Caspase 3/7 Green Invitrogen R37111 50
 CFSE Invitrogen C34554 20000
 CellTraceViolet Invitrogen C34557 10000
 CellTraceYellow Invitrogen C34567 10000

Isotype controls were used at equimolar concentrations of the marker antibody

Validation

Antibodies were used following the manufacturer's instructions.

The antibodies used in this study were used according to the manufacturer's recommendation. Validation was based on the description provided on the manufacturer's homepage.

Marker /Fluorochrome/ Clone /Company /Reference/Link

B7-H6 PE B7-H6 PE 875001 FAB7144P-100 R&D Systems https://www.rndsystems.com/products/human-b7-h6-pe-conjugated-antibody-875001_fab7144p

CD107a BV605 H4A3 BioLegend 328634 <https://www.biolegend.com/de-de/products/brilliant-violet-605-anti-human-cd107a-lamp-1-antibody-8975>

CD158 (KIR2D) BUV395 HP-MA4 BD 567326 https://www.bdbiosciences.com/en-eu/products/reagents/flow-cytometry-reagents/research-reagents/single-color-antibodies-ruo/buv395-mouse-anti-human-kir2dl1-s1-s3-s5-cd158.567326?tab=product_details

CD3 BUV805 SK7 BD 612894 https://www.bdbiosciences.com/en-eu/products/reagents/flow-cytometry-reagents/research-reagents/single-color-antibodies-ruo/buv805-mouse-anti-human-cd3.612894?tab=product_details

CD3 BV510 OKT3 BioLegend 317332 <https://www.biolegend.com/de-de/products/brilliant-violet-510-anti-human-cd3-antibody-8009>

CD45 PE-CF594 HI30 BD 562279 https://www.bdbiosciences.com/en-eu/products/reagents/flow-cytometry-reagents/research-reagents/single-color-antibodies-ruo/pe-cf594-mouse-anti-human-cd45.562279?tab=product_details

CD45 AF700 HI30 BioLegend 304023/4 <https://www.biolegend.com/de-de/products/alexa-fluor-700-anti-human-cd45-antibody-3401>

CD45 PEDzzle 2D1 BioLegend 368529/30 <https://www.biolegend.com/de-de/products/pe-dazzle-594-anti-human-cd45-antibody-14705>

CD69 RB744 FN50 BD 570501 https://www.bdbiosciences.com/en-eu/products/reagents/flow-cytometry-reagents/research-reagents/single-color-antibodies-ruo/rb744-mouse-anti-human-cd69.570501?tab=product_details

CD69 BV605 FN50 BioLegend 310937/8 <https://www.biolegend.com/de-de/products/brilliant-violet-605-anti-human-cd69-antibody-8704>

CD69 PERCPy5.5 FN50 BioLegend 310925 <https://www.biolegend.com/de-de/products/percp-cyanine5-5-anti-human-cd69-antibody-5606>

CD94 PE HP-3D9 BD 555889 <https://www.bdbiosciences.com/en-eu/products/reagents/flow-cytometry-reagents/research-reagents/>

single-color-antibodies-ruo/pe-mouse-anti-human-cd94.555889?tab=product_details
 CD96 APC NK92.39 BioLegend 338409 <https://www.biolegend.com/de-de/products/apc-anti-human-cd96-tactile-antibody-12180>
 CD96 BV421 6F9 BD 742794 https://www.bdbiosciences.com/en-eu/products/reagents/flow-cytometry-reagents/research-reagents/single-color-antibodies-ruo/bv421-mouse-anti-human-cd96.742794?tab=product_details
 CD96 PercpCy5.5 NK92.39 BioLegend 338411 <https://www.biolegend.com/de-de/products/percp-cyanine5-5-anti-human-cd96-tactile-antibody-12181>
 CTLA4/CD152 RY586 BNI3 BD 568442 https://www.bdbiosciences.com/en-eu/products/reagents/flow-cytometry-reagents/research-reagents/single-color-antibodies-ruo/ry586-mouse-anti-human-cd152.568442?tab=product_details
 DNAM1 FITC 11A8 BioLegend 338304 <https://www.biolegend.com/de-de/products/fitc-anti-human-cd226-dnam-1-antibody-5544>
 DNAM-1 BV711 11A8 BioLegend 338333 <https://www.biolegend.com/de-de/products/brilliant-violet-711-anti-human-cd226-antibody-15592>
 Gzmb Pacific blue GB11 BioLegend 515408 <https://www.biolegend.com/de-de/products/pacific-blue-anti-human-mouse-granzyme-b-antibody-8612>
 IFNg APC 4S.B3 Invitrogen 17-7319-82 <https://www.thermofisher.com/antibody/product/IFN-gamma-Antibody-clone-4S-B3-Monoclonal/17-7319-82>
 IFNg APC 4S.B3 BioLegend 502512 <https://www.biolegend.com/de-de/products/apc-anti-human-ifn-gamma-antibody-1012>
 IFNg PercpCy5.5 4S.B3 BioLegend 502526 <https://www.biolegend.com/de-de/products/percp-cyanine5-5-anti-human-ifn-gamma-antibody-4426>
 KLRG1 RB780 Z7-205.rMAb BD 569137 https://www.bdbiosciences.com/en-eu/products/reagents/flow-cytometry-reagents/research-reagents/single-color-antibodies-ruo/rb780-mouse-anti-human-klrg1.569137?tab=product_details
 LAG-3 APC-R700 T47-530 BD 565775 https://www.bdbiosciences.com/en-eu/products/reagents/flow-cytometry-reagents/research-reagents/single-color-antibodies-ruo/apc-r700-mouse-anti-human-lag-3-cd223.565775?tab=product_details
 LAG-3 APC 3DS223H Invitrogen 17-2239-42 <https://www.thermofisher.com/antibody/product/CD223-LAG-3-Antibody-clone-3DS223H-Monoclonal/17-2239-42>
 Mouse CD11b APCCy7 M1/70 BioLegend 101226 <https://www.biolegend.com/de-de/products/apc-cyanine7-anti-mouse-human-cd11b-antibody-3930>
 Mouse CD11b BV711 M1/70 BioLegend 101241 <https://www.biolegend.com/de-de/products/brilliant-violet-711-anti-mouse-human-cd11b-antibody-7927>
 MICA/B BV711 6D4 BD 742326 https://www.bdbiosciences.com/en-eu/products/reagents/flow-cytometry-reagents/research-reagents/single-color-antibodies-ruo/bv711-mouse-anti-human-mic-a-b.742326?tab=product_details
 mouseCD45 PEDdzzle 30-F11 BioLegend 103146 <https://www.biolegend.com/de-de/products/pe-dazzle-594-anti-mouse-cd45-antibody-10070>
 mouseCD45 BV510 30-F11 BioLegend 103137 <https://www.biolegend.com/de-de/products/brilliant-violet-510-anti-mouse-cd45-antibody-7995>
 Nectin-2 APC TX31 BioLegend 337412 <https://www.biolegend.com/de-de/products/apc-anti-human-cd112-nectin-2-antibody-11898>
 Nectin-2 Percp-Cy5.5 TX31 BioLegend 337415 <https://www.biolegend.com/de-de/products/percp-cyanine5-5-anti-human-cd112-nectin-2-antibody-11881>
 NKG2a BB700 131411 BD 747926 https://www.bdbiosciences.com/en-eu/products/reagents/flow-cytometry-reagents/research-reagents/single-color-antibodies-ruo/bb700-mouse-anti-human-nkg2a-cd159a.747926?tab=product_details
 NKG2D BV421 1D11 BioLegend 320822 <https://www.biolegend.com/de-de/products/brilliant-violet-421-anti-human-cd314-nkg2d-antibody-12395>
 NKG2D BV785 1D11 BioLegend 320830 <https://www.biolegend.com/de-de/products/brilliant-violet-785-anti-human-cd314-nkg2d-antibody-15537>
 NKG2D PECy7 1D11 BioLegend 320812 <https://www.biolegend.com/de-de/products/pe-cyanine7-anti-human-cd314-nkg2d-antibody-6499>
 Nkp30 BUV737 P30-15 BD 749128 https://www.bdbiosciences.com/en-eu/products/reagents/flow-cytometry-reagents/research-reagents/single-color-antibodies-ruo/buv737-mouse-anti-human-cd337-nkp30.749128?tab=product_details
 Nkp30 APC P30-15 BioLegend 325210 <https://www.biolegend.com/de-de/products/apc-anti-human-cd337-nkp30-antibody-3856>
 Nkp44 BUV615 P44-8 BD 752353 https://www.bdbiosciences.com/en-eu/products/reagents/flow-cytometry-reagents/research-reagents/single-color-antibodies-ruo/buv615-mouse-anti-human-nkp44-cd336.752353?tab=product_details
 Nkp46 AF647 9E2 BioLegend 331910 <https://www.biolegend.com/de-de/products/alexa-fluor-647-anti-human-cd335-nkp46-antibody-4578>
 PD1 APCCy7 EH12.2H7 BioLegend 329921 <https://www.biolegend.com/de-de/products/apc-cyanine7-anti-human-cd279-pd-1-antibody-7121>
 PD1 BV480 EH12.1 BD 566112 https://www.bdbiosciences.com/en-eu/products/reagents/flow-cytometry-reagents/research-reagents/single-color-antibodies-ruo/bv480-mouse-anti-human-cd279-pd-1.566112?tab=product_details
 PD1 FITC MIH4 Invitrogen 11-9969-42 <https://www.thermofisher.com/antibody/product/CD279-PD-1-Antibody-clone-MIH4-Monoclonal/11-9969-42>
 PD-L1 APC 29E.2A3 BD 568315 https://www.bdbiosciences.com/en-eu/products/reagents/flow-cytometry-reagents/research-reagents/single-color-antibodies-ruo/apc-mouse-anti-human-pd-l1-cd274.568315?tab=product_details
 Perforin BV711 dG9 Sony 2140645 <https://www.sonybiotechnology.com/gb/brilliant-violet-711tm-anti-human-perforin>
 PVR PECy7 SKII.4 BioLegend 337614 <https://www.biolegend.com/de-de/products/pe-cyanine7-anti-human-cd155-pvr-antibody-11925>
 TIGIT PECy7 A15153G BioLegend 372713 <https://www.biolegend.com/de-de/products/pe-cyanine7-anti-human-tigit-vstm3-antibody-13951>
 TIGIT PercpCy5.5 A15153G BioLegend 372717 <https://www.biolegend.com/de-de/products/percp-cyanine5-5-anti-human-tigit-vstm3-antibody-13948>
 TIM3 BV650 7D3 BD 565564 https://www.bdbiosciences.com/en-eu/products/reagents/flow-cytometry-reagents/research-reagents/single-color-antibodies-ruo/bv650-mouse-anti-human-tim-3-cd366.565564?tab=product_details
 TNF BUV395 Mab11 BD 563996 https://www.bdbiosciences.com/en-eu/products/reagents/flow-cytometry-reagents/research-reagents/single-color-antibodies-ruo/buv395-mouse-anti-human-tnf.563996?tab=product_details
 TNF PECy7 Mab11 BioLegend 502930 <https://www.biolegend.com/de-de/products/pe-cyanine7-anti-human-tnf-alpha-antibody-6515>
 ULBP-1 PERCP 170818 R&D Systems FAB1380C https://www.rndsystems.com/products/human-ulbp-1-percp-conjugated-antibody-170818_fab1380c
 ULBP-2/5/6 BV605 165903 BD 748131 https://www.bdbiosciences.com/en-eu/products/reagents/flow-cytometry-reagents/research-reagents/single-color-antibodies-ruo/bv605-mouse-anti-human-ulbp-2-5-6.748131?tab=product_details

ULBP3 AF405 166510 R&D Systems FAB1517V https://www.rndsystems.com/products/human-ulbp-3-alexa-fluor-405-conjugated-antibody-166510_fab1517v

ULBP-4 AF750 709116 R&D Systems FAB6285S https://www.rndsystems.com/products/human-ulbp-4-raet1e-alexa-fluor-750-conjugated-antibody-709116_fab6285s

Vd1 PE REA173 Miltenyi 130-120-440 <https://www.miltenyibiotec.com/US-en/products/tcr-vd1-antibody-anti-human-reafinity-rea173.html#Conjugate=PE:size=100-tests-in-200-ul>

Vd1 FITC REA173 Miltenyi 130-118-362 <https://www.miltenyibiotec.com/US-en/products/tcr-vd1-antibody-anti-human-reafinity-rea173.html#Conjugate=PE:size=100-tests-in-200-ul>

Vd1 APC REA173 Miltenyi 130-119-145 <https://www.miltenyibiotec.com/UN-en/products/tcr-vd1-antibody-anti-human-reafinity-rea173.html#conjugate=apc:size=100-tests-in-200-ul>

Vd2 APC-Vio770 REA771 Miltenyi 130-111-130 <https://www.miltenyibiotec.com/UN-en/products/tcr-vd2-antibody-anti-human-reafinity-rea771.html#Conjugate=APC-Vio-770:size=30-tests-in-60-ul>

IgG1 BV785 MOPC-21 BioLegend 400169 <https://www.biolegend.com/de-de/products/brilliant-violet-785-mouse-igg1-kappa-isotype-ctrl-7955>

IgG1 BV711 MOPC-21 BioLegend 400167 <https://www.biolegend.com/de-de/products/brilliant-violet-711-mouse-igg1-kappa-isotype-ctrl-7930>

IgG1 BV421 X40 BioLegend 400157 <https://www.biolegend.com/en-gb/products/brilliant-violet-421-mouse-igg1-kappa-isotype-ctrl-7194?GroupID=BLG15288>

IgG1 BV650 X40 BD 563231 https://www.bdbiosciences.com/en-pt/products/reagents/flow-cytometry-reagents/research-reagents/flow-cytometry-controls-and-lysates/bv650-mouse-igg1-k-isotype-control.563231?tab=product_details

IgG1 FITC MOPC-21 BioLegend 400108 <https://www.biolegend.com/de-de/products/fitc-mouse-igg1-kappa-isotype-ctrl-1406>

IgG1 RB744 X40 BD 570519 https://www.bdbiosciences.com/en-pt/products/reagents/flow-cytometry-reagents/research-reagents/single-color-antibodies-ruo/rb744-mouse-igg1-isotype-control.570519?tab=product_details

IgG1 BV605 MOPC-21 BioLegend 400161 <https://www.biolegend.com/de-de/products/brilliant-violet-605-mouse-igg1-kappa-isotype-ctrl-7630>

IgG1 APC-R700 X40 BD 564974 https://www.bdbiosciences.com/en-pt/products/reagents/flow-cytometry-reagents/research-reagents/flow-cytometry-controls-and-lysates/apc-r700-mouse-igg1-isotype-control.564974?tab=product_details

IgG1 BUV737 X40 BD 612758 https://www.bdbiosciences.com/en-pt/products/reagents/flow-cytometry-reagents/research-reagents/flow-cytometry-controls-and-lysates/buv737-mouse-igg1-isotype-control.612758?tab=product_details

IgG1 PE MOPC-21 BioLegend 400112 <https://www.biolegend.com/de-de/products/pe-mouse-igg1-kappa-isotype-ctrl-1408>

IgG1 BUV615 X40 BD 612986 https://www.bdbiosciences.com/en-pt/products/reagents/flow-cytometry-reagents/research-reagents/flow-cytometry-controls-and-lysates/buv615-mouse-igg1-isotype-control.612986?tab=product_details

IgG1 RB780 X40 BD 568532 <https://www.bdbiosciences.com/en-pt/search-results?searchKey=568532>

IgG1 PercpCy5.5 MOPC-21 BioLegend 400149 <https://www.biolegend.com/de-de/products/percp-cyanine5-5-mouse-igg1-kappa-isotype-ctrl-4205>

IgG1 PECy7 MOPC-21 BioLegend 400125 <https://www.biolegend.com/de-de/products/pe-cyanine7-mouse-igg1-kappa-isotype-ctrl-1926>

IgG2a PECy7 MOPC-173 BioLegend 400232 <https://www.biolegend.com/de-de/products/pe-cyanine7-mouse-igg2a-kappa-isotype-ctrl-1924>

IgG2a BB700 G155-178 BD 566419 https://www.bdbiosciences.com/en-pt/products/reagents/flow-cytometry-reagents/research-reagents/flow-cytometry-controls-and-lysates/bb700-mouse-igg2a-isotype-control.566419?tab=product_details

IgG2a RY586 G155-178 BD 568131 https://www.bdbiosciences.com/en-pt/products/reagents/flow-cytometry-reagents/research-reagents/single-color-antibodies-ruo/ry586-mouse-igg2a-isotype-control.568131?tab=product_details

IgG2a AF405 20102 R&D Systems IC003V https://www.rndsystems.com/products/mouse-igg2a-alexa-fluor-405-conjugated-isotype-control_ic003v

IgG2a BV605 G155-178 BD 562778 https://www.bdbiosciences.com/en-pt/products/reagents/flow-cytometry-reagents/research-reagents/flow-cytometry-controls-and-lysates/bv605-mouse-igg2a-k-isotype-control.562778?tab=product_details

IgG2a BV711 G155-178 BD 563345 https://www.bdbiosciences.com/en-pt/products/reagents/flow-cytometry-reagents/research-reagents/flow-cytometry-controls-and-lysates/bv711-mouse-igg2a-isotype-control.563345?tab=product_details

IgG2b BUV395 27-35 BD 563558 https://www.bdbiosciences.com/en-pt/products/reagents/flow-cytometry-reagents/research-reagents/flow-cytometry-controls-and-lysates/buv395-mouse-igg2b-isotype-control.563558?tab=product_details

IgG2b APC MPC-11 BioLegend 400322 <https://www.biolegend.com/de-de/products/apc-mouse-igg2b-kappa-isotype-ctrl-1410>

IgG2b AF750 133303 R&D Systems IC0041S https://www.rndsystems.com/products/mouse-igg2b-alexa-fluor-750-conjugated-isotype-control_ic0041s

Eukaryotic cell lines

Policy information about [cell lines and Sex and Gender in Research](#)

Cell line source(s)	All CRC cell lines - COLO-320DM (ATCC CCL-220, female, STR profiling), DLD1 (ATCC CCL-221, male), HCT116 (ATCC CCL-247, male), HT-29 (ATCC HTB-38, female), SW480 (ATCC CCL-228, male) and SW620 (ATCC CCL-227, male) - were obtained from the American Type Culture Collection (ATCC). All cell lines were authenticated by ATCC by STR profiling.
Authentication	All CRC cell lines - COLO-320DM (ATCC CCL-220, female, STR profiling), DLD1 (ATCC CCL-221, male), HCT116 (ATCC CCL-247, male), HT-29 (ATCC HTB-38, female), SW480 (ATCC CCL-228, male) and SW620 (ATCC CCL-227, male) - were obtained from the American Type Culture Collection (ATCC). All cell lines were authenticated by ATCC by STR profiling.
Mycoplasma contamination	All cells were tested negative for mycoplasma contamination
Commonly misidentified lines (See ICLAC register)	No commonly misidentified cell lines were used in the study

Animals and other research organisms

Policy information about [studies involving animals](#); [ARRIVE guidelines](#) recommended for reporting animal research, and [Sex and Gender in Research](#)

Laboratory animals	Eight-to-fourteen weeks-old female non-obese diabetic mice transgenic for human IL-15 were acquired from Taconic (NOD.Cg-Prkdcscid Il2rgtm1Sug Tg(CMV-IL2/IL15)1-1Jic/JicTac). Mice were housed in rooms with a light-dark cycle of 14h/10h, temperature of 22-24 °C and relative humidity of 45-65% in SPF (specific pathogen free) animal rooms of the Gulbenkian Institute for Molecular Medicine Rodent Facility (Lisbon, Portugal).
Wild animals	The study does not involve wild animals
Reporting on sex	All the experiments were performed in female mice due to initial stock availability at the supplier. Although previous experience and pilot studies suggest a negligible effect of sex differences in these experiments, we cannot rule out a certain level of influence when using male mice.
Field-collected samples	The study does not involve field-collected samples.
Ethics oversight	Mouse experiments performed in this study were evaluated and approved by our institutional ethical committee (iMM-Orbea) and the national competent authority (DGAV) under the license number 0421/000/000/2023. Given that tumors grow intra-cecum, humane endpoints are defined based on the assessment of body condition and physical appearance and not on tumor size. In this study humane endpoints were not reached, since mice were euthanized for analysis before symptoms of disease were detected.

Note that full information on the approval of the study protocol must also be provided in the manuscript.

Plants

Seed stocks	n/a
Novel plant genotypes	n/A
Authentication	n/a

Flow Cytometry

Plots

Confirm that:

- The axis labels state the marker and fluorochrome used (e.g. CD4-FITC).
- The axis scales are clearly visible. Include numbers along axes only for bottom left plot of group (a 'group' is an analysis of identical markers).
- All plots are contour plots with outliers or pseudocolor plots.
- A numerical value for number of cells or percentage (with statistics) is provided.

Methodology

Sample preparation	Single cell suspensions were incubated in PBS with fluorescently labelled monoclonal antibodies against the different surface markers for 20 minutes at 4 °C in the dark. For intracellular markers (cytolytic granules and cytokines), cells were fixed and permeabilized for intracellular staining with Foxp3 staining buffer set (Invitrogen) following the manufacturer's instructions. When indicated, cells were stimulated with 0,2µg/mL PMA (Merck) + 1µg/mL Ionomycin (Merck) in the presence of 10µg/mL Brefeldin A (Merck) + 0.1% Monensin (Invitrogen) for 3 hours at 37 °C prior surface staining for the evaluation of functional intracellular markers.
Instrument	Flow cytometry acquisition was performed on a BD LSRFortessa X-20 Cell Analyzer (BD Biosciences), BD FACSymphony A5 SE (BD Biosciences) or Cytek Aurora (Cytek).
Software	Sample acquisition was performed with BD FACSDIVA software version 9.0. Data was analyzed with FlowJo 10 software (TreeStar). The FlowJo plugin X-shift was used to classify endogenous Vδ1 T cells in different clusters.
Cell population abundance	cell sorting was not used in this study

Gating strategy

For in vitro DOT cell analysis: FSC-A/SSC-A for lymphocytes, FSC-H/FSC-W for singlets, viability marker (neg) vs SSC-A for alive cells, and CD3+Vd1+cells. Then, phenotypic and functional markers were evaluated

For in vivo DOT cell infiltration/phenotype analyses: FSC-A/SSC-A for lymphocytes, FSC-H/FSC-W for singlets, viability marker (neg) vs SSC-A for alive cells, mouse-CD45(or CD11b) versus human CD45 for human lymphocytes (DOTs) and CD3+Vd1+cells. Then, phenotypic and functional markers were evaluated

For in vitro killing assay: FSC-A/SSC-A to exclude cell debris, FSC-H/FSC-W for singlets, CTV+ for tumor cells. Then apoptosis markers were evaluated

Isotype controls were used to determine the negative and positive population of the different markers.

Tick this box to confirm that a figure exemplifying the gating strategy is provided in the Supplementary Information.